bioRxiv preprint doi: https://doi.org/10.1101/2023.10.15.562427; this version posted November 20, 2023. The copyright holder for this preprint (which was not certified by peer review) is the author/funder. All rights reserved. No reuse allowed without permission.

Transitions in dynamical regime and neural mode underlie perceptual decision-making

Thomas Zhihao Luo[1,*,#], Timothy Doyeon Kim[1,*,#], Diksha Gupta[1,3], Adrian G. Bondy[1], Charles D. Kopec[1], Verity A. Elliot[1], Brian DePasquale[1,4], Carlos D. Brody[1,2,#]

[1]Princeton Neuroscience Institute, Princeton University, Princeton, NJ, USA
[2]Howard Hughes Medical Institute, Princeton University, Princeton, NJ, USA
[3]Present address: Sainsbury Wellcome Centre, University College London, London, UK
[4]Present address: Department of Biomedical Engineering, Boston University, Boston, MA, USA
*equal contribution
[#]Correspondence should be addressed to: T.Z.L. zhihaol@princeton.edu, T.D.K. tdkim@princeton.edu, or C.D.B. brody@princeton.edu

Abstract

Perceptual decision-making is the process by which an animal uses sensory stimuli to choose an action or mental proposition. This process is thought to be mediated by neurons organized as attractor networks[1,2]. However, whether attractor dynamics underlie decision behavior and the complex neuronal responses remains unclear. Here we use an unsupervised, deep learning-based method to discover decision-related dynamics from the simultaneous activity of neurons in frontal cortex and striatum of rats while they accumulate pulsatile auditory evidence. We show that contrary to prevailing hypotheses, attractors play a role only after a transition from a regime in the dynamics that is strongly driven by inputs to one dominated by the intrinsic dynamics. The initial regime mediates evidence accumulation, and the subsequent intrinsic-dominant regime subserves decision commitment. This regime transition is coupled to a rapid reorganization in the representation of the decision process in the neural population (a change in the "neural mode" along which the process develops). A simplified model approximating the coupled transition in the dynamics and neural mode allows inferring, from each trial's neural activity, the internal decision commitment time in that trial, and captures diverse and complex single-neuron temporal profiles, such as ramping and stepping[3–5]. It also captures trial-averaged curved trajectories[6–8], and reveals distinctions between brain regions. Our results show that the formation of a perceptual choice involves a rapid, coordinated transition in both the dynamical regime and the neural mode of the decision process, and suggest pairing deep learning and parsimonious models as a promising approach for understanding complex data.

Theories of attractor dynamics have been successful at capturing multiple brain functions[9], including motor planning[10] and neural representations of space[11,12]. Attractors are a set of states toward which a system tends to evolve, from a variety of starting positions. In these theories, the computations of a brain function are carried out by the temporal evolution, or the dynamics, of the system. Experimental findings support the idea that the brain uses systems with attractor states for computations underlying working memory[10] and navigation[11]. These theories often focus on the low-dimensional nature of neural population activity[6,7,13,14], and account for the responses across a large number of neurons using a dynamical system model whose variable has only a few dimensions[15,16,11,17].

Attractor network models have also been hypothesized to underlie perceptual decision-making: the process through which noisy sensory stimuli are categorized to select an action or mental proposition. In these hypotheses, the network dynamics carry out the computations needed in decision formation[1,6,18–26], such as accumulating sensory evidence and committing to a choice. While some experimental evidence favors a role of

bioRxiv preprint doi: https://doi.org/10.1101/2023.10.15.562427; this version posted November 20, 2023. The copyright holder for this preprint (which was not certified by peer review) is the author/funder. All rights reserved. No reuse allowed without permission.

attractors in perceptual decisions[10,27,28], the actual population-level dynamics underlying decision-making has been elusive. Knowledge of these dynamics would directly test the current prevailing attractor hypotheses, provide fundamental constraints on neural circuit models, and account for the often complex temporal profiles of neural activities.

A separate line of work involves tools, sometimes based on deep learning, for discovering, in a data-driven manner, the low-dimensional component of neural activity[14,29,30]. In this approach, the spike trains of many simultaneously recorded neurons are modeled as being a function of a few "latent" variables that are shared across neurons.

To combine both lines of work, we used a novel method[31] that estimates, from the spike trains of simultaneously recorded neurons, the dynamics of a low-dimensional variable $\boldsymbol{z}$, given by:

$$\dot{\boldsymbol{z}} = F(\boldsymbol{z}, \boldsymbol{u}) + \boldsymbol{\eta} \qquad (1)$$

where $\boldsymbol{u}$ are external inputs, $\boldsymbol{\eta}$ is noise, and, when applied to perceptual decisions, $\boldsymbol{z}$ represents the dynamical state of the brain's decision process at a given time (**Fig**. 1a-c). The instantaneous change of the decision variable, or its dynamics, is given by $\dot{\boldsymbol{z}}$, which depends on $\boldsymbol{z}$ itself, as well as $\boldsymbol{u}$ and $\boldsymbol{\eta}$. This approach aims to estimate the function F, and through it, capture the presence and nature of attractors in the neural dynamics.

Intrinsic and input dynamics differentiate hypotheses

The deterministic dynamics F (that is, in the absence of $\boldsymbol{\eta}$) is useful for distinguishing among attractor hypotheses of decision-making. F can be dissected into two components: the intrinsic (i.e., input-independent) dynamics and the input-driven dynamics. Intrinsic dynamics occur even in the absence of sensory inputs $\boldsymbol{u}$ (i.e., $F(\boldsymbol{z}, \boldsymbol{0})$; **Fig**. 1d; Extended Data Fig. 1a-b). Changes in $\boldsymbol{z}$ driven solely by sensory inputs $\boldsymbol{u}$ can be isolated from the intrinsic dynamics as $F(\boldsymbol{z}, \boldsymbol{u}) - F(\boldsymbol{z}, \boldsymbol{0})$ (**Fig**. 1e; Extended Data Fig. 1c-e).

Many of the currently prevailing neural attractor hypotheses of decision-making have been inspired by a classic and successful behavioral level model, the drift diffusion model (DDM)[32–34]. In the behavioral DDM, a scalar (i.e., one-dimensional) decision variable a is driven by sensory evidence inputs (Extended Data Fig. 8a-b). For example, for decisions between Go-Right versus Go-Left, momentary evidence for Right (Left) might drive a in a positive (negative) direction. Through these inputs, the momentary evidence is accumulated over time in a until the value of a reaches an absorbing bound, a moment thought to correspond to decision commitment, and after which inputs no longer affect a. Different bounds correspond to different choice options: a positive (negative) bound would correspond to the decision to Go-Right (Go-Left). A straightforward implementation of the DDM in neural population dynamics, which we will refer to as the "classic neural DDM," would posit a line attractor in neural space, with position of the neural state $\boldsymbol{z}$ along that line representing the value of a, and two point attractors at the ends of the line to represent the decision commitment bounds (**Fig**. 1g)[35]. Another hypothesis approximates the DDM process using bistable attractors[1], with each of the two attractors representing each of the decision bounds, and in between the two attractors, a one-dimensional manifold of slow intrinsic dynamics that corresponds to the evidence accumulation regime (**Fig**. 1f). In both the classic neural DDM and bistable attractor hypotheses, differential evidence inputs are aligned with the slow dynamics manifold and the attractors at its endpoints. A third hypothesis, inspired by trained recurrent neural networks (RNNs), also posits a line attractor (**Fig**. 1h), but allows for evidence inputs that are not aligned with the line attractor[6]. In all three hypotheses, intrinsic dynamics flow towards the line attractor/slow manifold (**Fig**. 1f,g). Because these three hypotheses were each designed to explain a particular set of the phenomena observed in decision-making experiments, a broader range of experimental observations could suggest dynamics that have not been previously hypothesized. As but one example, the intrinsic dynamics may contain

bioRxiv preprint doi: https://doi.org/10.1101/2023.10.15.562427; this version posted November 20, 2023. The copyright holder for this preprint (which was not certified by peer review) is the author/funder. All rights reserved. No reuse allowed without permission.

discrete attractors that do not lie at the endpoints of a one-dimensional slow dynamics manifold (**Fig**. 1i; Extended Data Fig. 1); many other arrangements are possible.

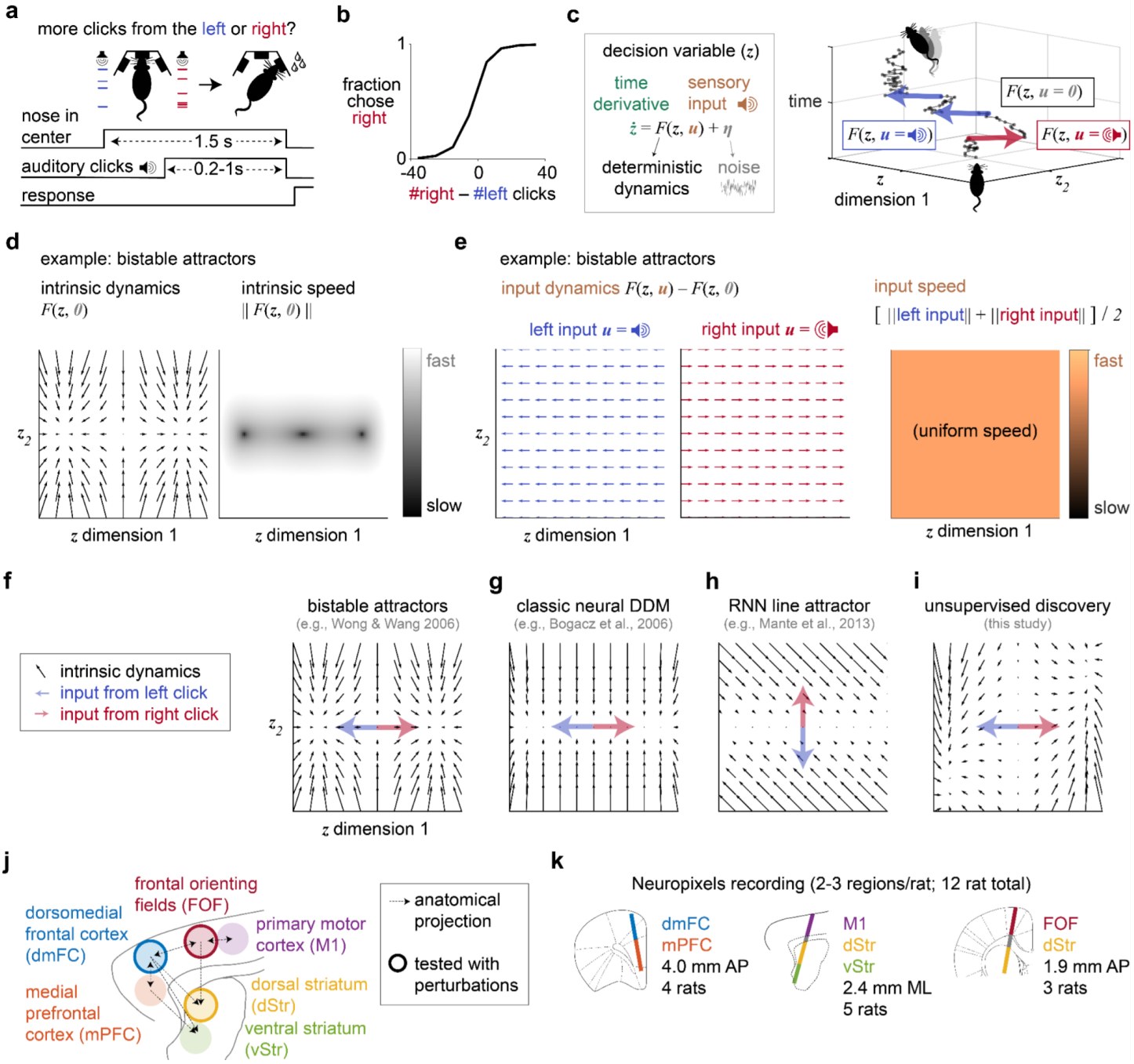

Figure 1. Attractor models of decision-making were tested by recording from rat frontal cortex and striatum. **a,** Rats were trained to accumulate auditory pulsatile evidence over time. While keeping its head stationary, the rat listened to randomly timed clicks played from loudspeakers on its left and right. At the end of the stimulus, the rat receives a water reward for turning to the side with more clicks. **b**, Behavioral performance in an example recording session. **c**, The decision process is modeled as a dynamical system. Right: the blue, red, and black lines represent the change in the decision variable in the presence of left, right, or no click, respectively. **d**, Intrinsic dynamics illustrated using the bistable attractors hypothesis. In the velocity vector field (i.e., flow field; left), the arrow at each value of the decision variable z indicates how the instantaneous change depends on z itself. The arrow's orientation represents the direction of the change, and its size the speed, which is also quantified using a heat map (right). **e**, Changes in z driven solely by the external sensory inputs. **f**,

bioRxiv preprint doi: https://doi.org/10.1101/2023.10.15.562427; this version posted November 20, 2023. The copyright holder for this preprint (which was not certified by peer review) is the author/funder. All rights reserved. No reuse allowed without permission.

Bistable attractors hypothesis of decision-making, with the directions of the input dynamics. **g**, A hypothesis supposing a line attractor in the intrinsic dynamics, based on the drift-diffusion model (DDM) of decision behavior. **h**, Recurrent neural networks (RNN) can be trained to make perceptual decisions using a line attractor that is not aligned to the input dynamics. **i**, An example of attractor dynamics that have not been previously hypothesized. **j**, Six interconnected frontal cortical and striatal regions are examined here. **k**, Neuropixels recordings (318±147 neurons/session/probe, mean±STD) from twelve rats.

Dissociating between intrinsic and input dynamics requires neural recordings during a decision unfolding over a time period that includes intervals both with and without momentary evidence inputs. We trained rats to perform a task in which they listened to randomly timed auditory pulses played from its left and right and reported the side where more pulses were played (**Fig**. 1a). The stochastic pulse trains allow us to sample neural responses time-locked to pulses, which are useful for inferring the input-driven dynamics, and also the neural activity in the intervals between pulses, which is useful for inferring the intrinsic dynamics. Expert rats are highly sensitive to small differences in the auditory pulse number (**Fig**. 1b; Extended Data Fig. 2a), and the behavioral strategy of rats in this task is typically well captured by gradual accumulation of evidence, which is at the core of the DDM[36,37].

While the rats performed this task, we recorded six frontal cortical and striatal regions with chronically implanted Neuropixels probes (**Fig**. 1j-k; Extended Data Fig. 2b). The frontal orienting fields (FOF) and anterior dorsal striatum (dStr) are known to be causally necessary for this task and are interconnected[38–40]. The dorsomedial frontal cortex (dmFC) is a major anatomical input to dStr[41], as confirmed by our retrograde tracing (Extended Data Fig. 2c) and is also causally necessary for the task (Extended Data Fig. 1d). The dmFC is interconnected with the medial prefrontal cortex (mPFC), and less densely, the FOF and the primary motor cortex (M1)[42], and provides inputs to the anterior ventral striatum (vStr)[41].

Unsupervised discovery reveals transitions in dynamical regime

To test the current attractor hypotheses and to allow discovery of dynamics that were not previously hypothesized, a flexible yet interpretable method is needed. We used a novel deep learning method (Flow-field Inference from Neural Data using deep Recurrent networks; FINDR[31]) that infers the low-dimensional stochastic dynamics that best account for population spiking data. The low-dimensionality of the description is critical for interpretability. Prominent alternative deep learning-based tools for inferring neural latent dynamics involve models in which these latent dynamics have hundreds of dimensions and are deterministic[29,43,44]. In contrast, FINDR infers latent dynamics that are low-dimensional and stochastic. The stochasticity in the latent dynamics accounts for noise in the decision process that contributes to errors. FINDR uses artificial neural networks as function approximators to infer the function F (Eq. 1; **Fig**. 1c). Specifically, the decision-related dynamics F are approximated with gated neural stochastic differential equations[45] (**Fig**. 2a). Each of the many neurons' firing rates at each timepoint is modeled as a weighted sum of the z variables, followed by a softplus nonlinearity, which can be thought of as approximating neuronal current-frequency curves[10] (**Fig**. 2b). The weighting for each neuron (vector $\boldsymbol{w}_n$ for neuron n, comprising the n-th row of a weight matrix $\boldsymbol{W}$; **Fig**. 2b) is fit to the data, and to aid the interpretability of z, we transform $\boldsymbol{W}$ post-training such that it acts as a rotation. This makes z preserve angles and distances in $\boldsymbol{W}z$ (neural space before softplus nonlinearity). Prior to applying FINDR, we separately account for the decision-independent, deterministic but time-varying baseline firing rate for each neuron ("baseline" in **Fig**. 2b), so that FINDR can focus directly on the choice formation process. We first confirmed that FINDR can indeed capture population dynamics on a trial by trial basis. FINDR provided a good fit to individual neurons' heterogeneous single-trial firing rates, as well as to the complex dynamics in their peristimulus time histograms (PSTH) given an evidence strength (Extended Data Fig. 4). We explored the

bioRxiv preprint doi: https://doi.org/10.1101/2023.10.15.562427; this version posted November 20, 2023. The copyright holder for this preprint (which was not certified by peer review) is the author/funder. All rights reserved. No reuse allowed without permission.

number of dimensions in the latent dynamics that best captures our data, and found this to be two (Extended Data Fig. 5). Focusing on the low-dimensional velocity vector fields (i.e., flow fields) with which FINDR describes the multi-neuron population dynamics, we confirmed that in synthetic data, FINDR-inferred vector fields can be used to distinguish between competing dynamical systems hypotheses of perceptual decision-making (Extended Data Fig. 3). After these validations, we turned to examining the vector fields estimated by FINDR from the recorded spiking data.

Fig. 2c-h illustrates a representative recording session from dmFC and mPFC. Similar results for further sessions and brain regions are shown in Extended Data Fig. 6. Notably, the configuration of intrinsic and input dynamics inferred by FINDR is not consistent with any of the existing attractor hypotheses. As in the bistable attractor hypothesis[1,19] (**Fig**. 1d-f), we find two attractors and one unstable fixed point, with each attractor corresponding to one of the two possible alternatives. But in the bistable attractor hypothesis, as well as the other hypotheses illustrated in **Fig**. 1 and indeed all other hypotheses we are aware of, the intrinsic dynamics play an important role throughout the entire decision-making process. In contrast, at least within the space of the latent variable z, the FINDR-inferred dynamics suggest that initially, motion in neural space is dominated and driven by the inputs to decision-making regions (i.e., by the input-dependent dynamics), not the intrinsic dynamics (**Fig**. 2c-h; although we do note that the intrinsic dynamics at the origin are consistently inferred to be a weakly unstable point). Later in the decision-making process, the balance between intrinsic versus input-driven dynamics inverts and it is the intrinsic dynamics that become dominant. **Fig**. 2g plots the difference in magnitude between the intrinsic minus input-driven dynamics (indicated with the color scale), on the plane of the latent dimensions z. The initial dominance of the input-driven dynamics can be seen in the large zone near the (0,0) origin of the latent dimensions, at the negative end of the color scale. The later dominance of the intrinsic dynamics can be seen in the right and left edges of the sampled region, which are reached later in the decision-making process, and which are at the opposite end of the color scale. Moreover, in another significant difference with the bistable attractor hypothesis, the direction of instantaneous change driven by the inputs (slightly clockwise from the horizontal in **Fig**. 2e) is not aligned with the axis formed by the two attractors (slightly clockwise from vertical in **Fig**. 2c-d). These overall features were observed across rats and behavioral sessions (Extended Data Fig. 6).

Unsupervised inference of dynamics underlying decision-making, based only on spiking activity and sensory evidence inputs, thus suggests that the process unfolds in two separate sequential regimes. In the initial regime, the dynamics are largely determined by the inputs, with intrinsic dynamics playing only a minor role. The inputs from sensory evidence (right and left clicks) drive the decision variable to evolve along an axis, parallel to the directions of the input dynamics, that we will term the “evidence accumulation axis.” In a second, later regime, these characteristics reverse, the trajectories representing the evolution of the decision variable become largely independent of the inputs, and are instead mostly determined by the intrinsic dynamics. The intrinsic dynamics lead towards one of two attractors, which correspond to the two choice options in our behavioral task. We will term the straight line between the two attractors the “decision commitment” axis. Of note, the evidence accumulation axis and the decision commitment axis are almost orthogonal to each other. During the regime transition, the trajectories in z veer from evolving along the evidence accumulation axis to developing along the decision commitment axis. In neural space, this will equate to a transition from evolving along one “mode” (i.e., a direction in neural space) corresponding to evidence accumulation, to another mode, corresponding to decision commitment.

Also of note, in the initial regime, the intrinsic dynamics are slow along both of these axes, not only one. This latter feature, as pointed out above, contrasts with the hypotheses sketched in **Fig**. 1f-h: in all three of them, there are slow intrinsic dynamics, for evidence accumulation, only along a single one-dimensional line (the line attractor for the classic neural DDM and the RNN line attractor, and the slow manifold for the bistable attractor). Our findings here suggest instead that the slow intrinsic dynamics are on a two-dimensional manifold spanned by the evidence accumulation and the decision commitment axes.

bioRxiv preprint doi: https://doi.org/10.1101/2023.10.15.562427; this version posted November 20, 2023. The copyright holder for this preprint (which was not certified by peer review) is the author/funder. All rights reserved. No reuse allowed without permission.

Although derived entirely from unsupervised analysis of neural spiking activity and auditory click times, these two regimes are reminiscent of the two regimes of the behavioral DDM: namely, an initial regime in which momentary sensory inputs drive changes in the state of a scalar decision variable a, and a later regime, after a reaches a bound, in which the state becomes independent of the sensory inputs (Extended Data Fig. 8a-b). The correspondence between the two regimes inferred from spiking activity and the behavioral DDM suggests that a modified neural implementation of the DDM, focusing on key aspects of the two regimes, could be a simple model that captures many aspects of the neural data, while having far fewer parameters than FINDR and thus greater statistical power. We next develop this model, and show that it can be used to infer the subject's internal decision commitment time on each trial.

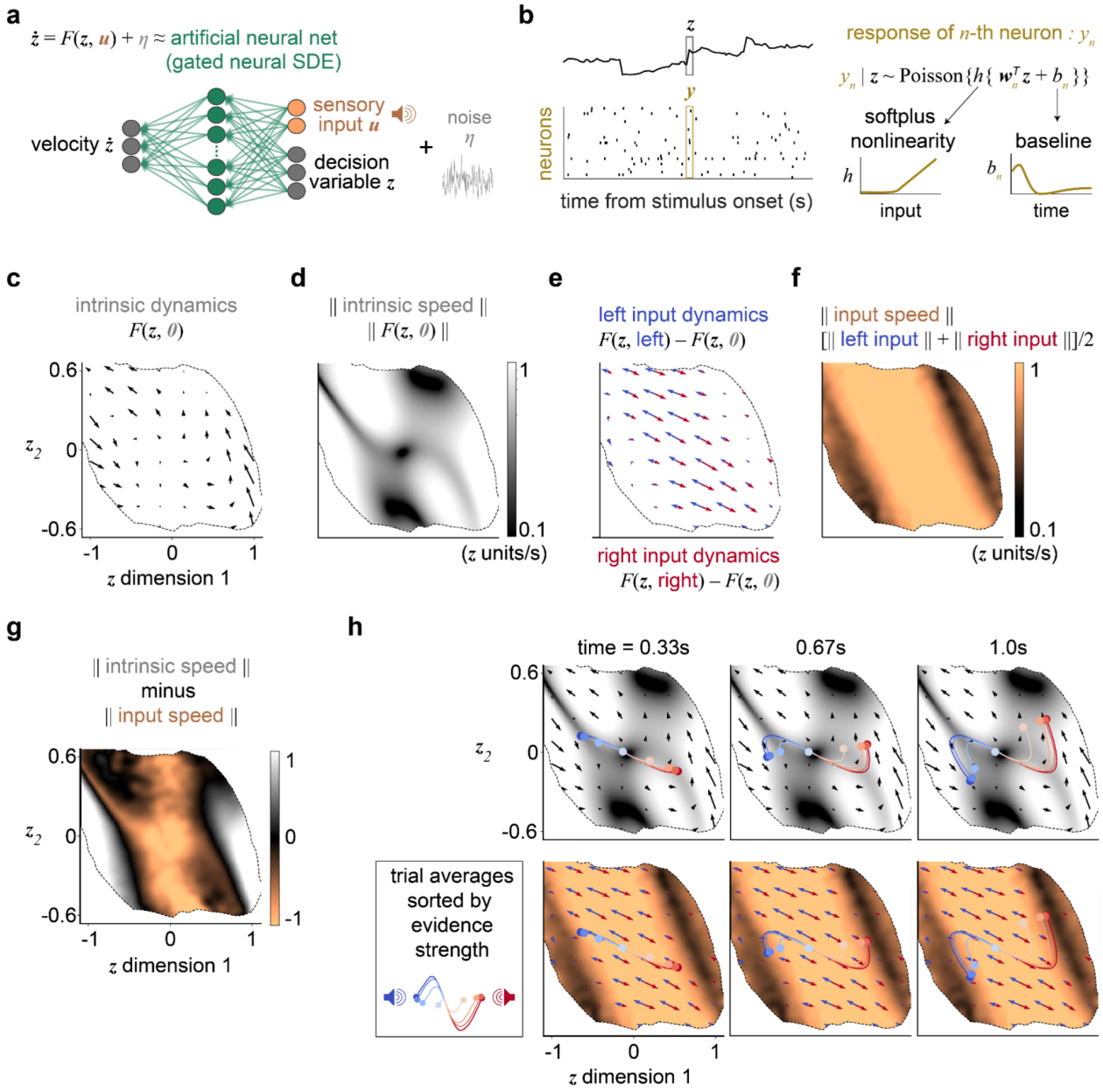

Figure 2. Unsupervised discovery reveals a coordinated transition in both the dynamical regime and neural representation that underlie the shift from evidence accumulation to decision commitment. **a**, The decision-related dynamics are approximated with an artificial neural network (gated neural stochastic differential equations; gnSDE) and inferred using the method "Flow-field Inference from Neural Data using deep Recurrent networks" (FINDR)[31]. The deterministic component F is approximated using a gated

bioRxiv preprint doi: https://doi.org/10.1101/2023.10.15.562427; this version posted November 20, 2023. The copyright holder for this preprint (which was not certified by peer review) is the author/funder. All rights reserved. No reuse allowed without permission.

feedforward network, and stochasticity $\boldsymbol{\eta}$ is modeled as a Gaussian with diagonal covariance. **b**, The parameters of the gnSDE are fit so that the value of the decision variable z can best capture the spike trains of simultaneously recorded neurons. Conditioned on the decision variable at each time step, the spiking response of each neuron at that time is modeled as a Poisson random variable. A softplus nonlinearity is used to approximate the threshold-linear frequency-current curve observed in cortical neurons during awake behavior. A baseline temporal function is learned for each neuron to account for the decision-irrelevant component of the neuron's response. **c-h**, Vector field inferred from a representative recording session from 67 choice-selective neurons in dmFC and mPFC. At each time point, only the well-sampled subregion of the state space (the portion occupied by at least 100 of 5000 simulated trial trajectories) is shown. **c**, Intrinsic dynamics. **d**, Speed of the intrinsic dynamics. **e**, Input dynamics of either a left or right click. Unlike sensory stimuli that are continuous over time, such as the random dot motion patches[46], the stimulus $\boldsymbol{u}$ in our task is pulsatile. If $\boldsymbol{u}=[1;0]$ indicates the input to be a single left click, $F(z, \boldsymbol{u}=[1;0]) - F(z, \boldsymbol{0})$ gives the input dynamics *given* that the input was a single left click. However, the left input dynamics depends on the frequency a left click, given by $p(\boldsymbol{u}=[1;0]|z)$. Therefore, we compute the left input dynamics $F(z, \text{left}) - F(z, \boldsymbol{0})$ as $p(\boldsymbol{u}=[1;0]|z)[F(z, \boldsymbol{u}=[1;0]) - F(z, \boldsymbol{0})]$. We similarly compute the right input dynamics $F(z, \text{right}) - F(z, \boldsymbol{0})$, with $\boldsymbol{u}=[0;1]$ indicating that input was a single right click. **f**, Speed of the input dynamics. **g**, The strength of the input-driven and intrinsic dynamics differ across the decision state-space: the input-driven dynamics are far stronger near the origin, whereas the intrinsic dynamics are far stronger in the periphery. These differences indicate the decision state-space to be approximately partitioned into two separate regimes: one in which the inputs drive the accumulation of evidence and another in which the intrinsic dynamics mediate the commitment to a choice and its maintenance in working memory. Difference in the speed between intrinsic and input dynamics. **h**, Initially, the trajectories representing the evolutions of the decision variable are strongly driven by inputs and develop along an axis parallel to the direction of the input dynamics, which we term the "evidence accumulation axis." At a later time, the trajectories become largely insensitive to the inputs, and are instead driven by the intrinsic dynamics to evolve along an axis in neural space, defined by the two discrete attractors, which we term the "decision commitment axis."

Simplified model of coordinated transitions in dynamical regime and neural mode

The FINDR-inferred vector fields suggest a rapid transition from a strongly input-driven regime to an intrinsic-dominant regime that is conceptually similar to the transition from evidence accumulation to decision commitment regimes of the behavioral DDM (**Fig.** 3a-b). The behavioral DDM is applied to a wide range of decision-making tasks, including tasks in which the stimulus duration is determined by the environment[36,39,47,48] as used here. This raises the possibility that the FINDR-inferred dynamics may be approximated by a simplified model in which the decision variable behaves exactly the same as in the behavioral DDM.

The regime transition coincides with a rapid reorganization in the representation of the decision process in the neural population. To quantify this reorganization, we can consider the activity of each neuron as a dimension in space, and an axis in this neural space as a "neural mode." Seen in this way, the regime change from evidence accumulation to decision commitment is coordinated with a fast transition in the neural mode. The proposal is conceptually similar to the rapid change in neural modes from motor preparation to motor execution[49]. Therefore, we ask whether a simplified model based on the idea of a rapid, coordinated transition in dynamical regime and neural mode can capture the key features of FINDR-inferred dynamics as well as a broad range of experimental observations.

In what we will call the multi-mode drift-diffusion model (MMDDM), a scalar decision variable z evolves as in the behavioral DDM, governed by three parameters (Extended Data Fig. 7a-b; **Fig**. 3b), but neurons

bioRxiv preprint doi: https://doi.org/10.1101/2023.10.15.562427; this version posted November 20, 2023. The copyright holder for this preprint (which was not certified by peer review) is the author/funder. All rights reserved. No reuse allowed without permission.

encode this decision variable in a different way before and after the decision commitment bound is reached (**Fig**. 3c). For each neuron, two scalar weights, w_{EA} and w_{DC}, specify the strength of its encoding of z during the evidence accumulation state (i.e., before reaching the bound, w_{EA}) and the decision commitment state (i.e., after reaching the bound, w_{DC}). When w_{EA} and w_{DC} are constrained to be the same, the MMDDM reduces to the classic neural DDM. Because neurons multiplex both decision-related and unrelated signals[50,51], MMDDM accounts for spike history and, as with FINDR, decision-unrelated baseline changes (Extended Data Fig. 7d-g). All parameters are learned simultaneously by jointly fitting to all spike trains and behavioral choices.

While the classic neural DDM captures ramp-like neuronal temporal profiles (Extended Data Fig. 8), the MMDDM can account for a broader range of neuronal profiles (**Fig**. 3d-h). For the vast majority of recording sessions, the data are better fit by the MMDDM than the classic neural DDM (cross-validated; **Fig**. 3i). The goodness-of-fit of the neuronal temporal profiles is improved by the MMDDM (**Fig**. 3j). We confirmed that the choices can be well predicted (**Fig**. 3k; Extended Data Fig. 7i) and that the vector fields inferred from real spike trains approximately match the vector fields inferred from the spike trains simulated by the MMDDM (**Fig**. 3l). Additional validations are shown in Extended Data Fig. 7j-n.

The state transition from evidence accumulation to decision commitment in the MMDDM, and a consequent switch from w_{EA} to w_{DC}, is reminiscent of the gradual change in neural modes encoding a decision variable to those encoding an action plan[7,52,53]. The MMDDM provides the further advantage of allowing precise inference of each trial's moment of the switch (the time of internal commitment to a decision), based on the recorded neural activity. A core prediction of the MMDDM is that if indeed it correctly infers the time of internal decision commitment, then we should be able to observe the contribution of the auditory click inputs to the behavioral choice ceasing abruptly at the estimated decision commitment time. This prediction can be tested by aligning each trial to the MMDDM-inferred time of decision commitment, and then measuring the time-varying weight of the stimulus fluctuations on the behavioral choice (referred to as the psychophysical kernel[54–56]). We used a logistic regression model to estimate the weight of each timepoint's auditory clicks on the subject's behavioral choice. Remarkably, consistent with the MMDDM prediction, the psychophysical weight of stimulus fluctuations abruptly diminishes to zero after the MMDDM-inferred time of commitment (**Fig**. 3m; Extended Data Fig. 9). Because these commitment times are broadly distributed in different trials (Extended Data Fig. 9k), if we instead align trials to the stimulus onset, the abrupt change is no longer observable, and we obtain a smooth psychophysical kernel (Extended Data Fig. 9e).

bioRxiv preprint doi: https://doi.org/10.1101/2023.10.15.562427; this version posted November 20, 2023. The copyright holder for this preprint (which was not certified by peer review) is the author/funder. All rights reserved. No reuse allowed without permission.

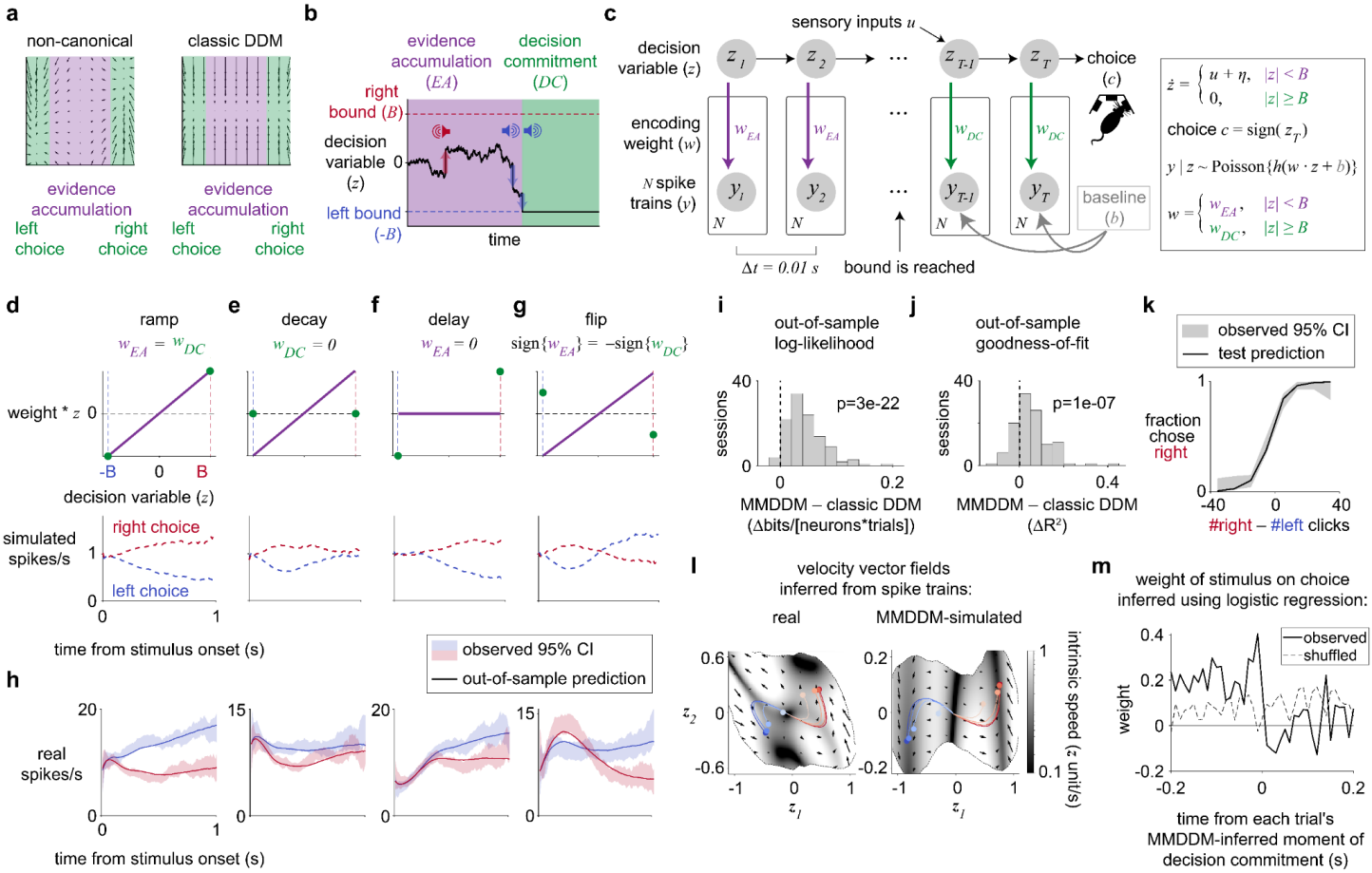

Figure 3. Multi-mode drift-diffusion model (MMDDM): a simplified model of discovered dynamics. **a**, The state space of both discovered dynamics and the classic neural DDM can be partitioned into an evidence accumulation regime and a decision commitment regime. **b**, The decision commitment regime of the classic neural DDM corresponds to the decision variable being at an absorbing bound. **c**, Directed graph of the MMDDM for a trial with T time steps and N simultaneously recorded neurons. The decision variable (z)'s time derivative ($\dot{z}$) depends on the input (u) and Gaussian noise (η) when its magnitude is less than bound B. The behavioral choice (c) is the sign of the decision variable at the last time step. The mapping from z to spike train response (y) passes through the softplus nonlinearity h and depends on baseline b and encoding weight w. The encoding weight is either w_{EA} and w_{DC} depending on z. **d**, The ramp temporal profile in a neuron's PSTH can be generated by setting w_{EA} and w_{DC} to be the same. **e**, The decay profile is simulated by setting w_{DC} to zero because as time passes, it is more and more likely to reach the bound and for the encoding to be mediated by w_{DC} rather than by w_{EA}. When w_{DC} is zero, there can be no selectivity. **f**, A delay profile is generated by setting w_{EA} to zero because the probability of reaching the bound is zero for some time after stimulus onset. **g**, The flip profile is produced by setting w_{EA} and w_{DC} to have opposite signs. **h**, For actual neurons, the MMDDM captures the diversity in choice-related temporal profiles. **i**, The MMDDM has a higher out-of-sample likelihood than the classic neural DDM. **j**, The MMDDM achieves a higher goodness-of-fit (coefficient-of-determination, R^2) of the choice-conditioned PSTH's than the classic neural DDM. **k**, Behavioral choices are well predicted. **l**, The vector field inferred from real spike trains is confirmed to be similar to that inferred from MMDDM-simulated spike trains. **m**, Consistent with a decision commitment state, the psychophysical weight of the stimulus on the behavioral choice decreases to near zero after time of decision commitment.

bioRxiv preprint doi: https://doi.org/10.1101/2023.10.15.562427; this version posted November 20, 2023. The copyright holder for this preprint (which was not certified by peer review) is the author/funder. All rights reserved. No reuse allowed without permission.

Abrupt and gradual changes at decision commitment

Perceptual decision-making involves a puzzling diversity in the temporal profiles of choice-selective neurons, with some displaying a ramp-to-bound profile, others exhibiting step-like profile, and some falling in between a ramp and a step[3–5]. This diversity might be explained by a rapid reorganization in population activity at the time of decision commitment. Not all neurons would be equally coupled to this change: a neuron similarly engaged in evidence accumulation and decision commitment would exhibit a ramp-to-bound profile, whereas a neuron more strongly engaged in commitment would show a steep–almost discontinuous–step. Moreover, neurons that are more strongly engaged in accumulation would reflect a ramp-and-decline profile. Can the changes in neuronal responses around the time of decision commitment explain the continuum of ramping and stepping profiles?

We find evidence for these predictions when we grouped neurons by whether they are more, less, or similarly engaged in evidence accumulation relative to decision commitment (Methods; **Fig**. 4a-d; Extended Data Fig. 10a). The peri-commitment neural response time histogram (PCTH) averaged across neurons similarly engaged in accumulation and commitment shows a ramp-to-bound profile. The PCTH resembles a step for the neurons more engaged in commitment, and shows a ramp-and-decline profile for neurons more engaged in accumulation. Even without grouping neurons, we find support for these predictions in the principal component analysis (PCA) on the PCTH's (Methods; **Fig**. 4e). The first three principal components correspond to the ramp-to-bound, step, and ramp-and-decline profiles. These results show that concurrent gradual and abrupt changes in neural responses around the time of decision commitment explain the continuum of ramp-to-bound and discrete step-like profiles.

Abrupt changes at decision commitment appear inconsistent with a phenomenon that is observed in many studies of decision-making: smoothly curved trial-averaged trajectories in low-dimensional neural state space[6–8]. Similar phenomena are observed in our data: the trial-averaged trajectories for left and right choices do not separate from each other along a straight line, but rather along curved arcs (**Figs**. 2h, 4f). These smoothly curving arcs may result from averaging over trajectories with an abrupt turn aligned to decision commitment, which occur at different times across trials (Extended Data Fig. 9k). Consistent with this account, the smooth curves in low-dimensional neural state space can be well captured by the out-of-sample predictions of MMDDM (**Fig**. 4g; Extended Data Fig. 11), but not the classic neural DDM (**Fig**. 4h). These results indicate that the MMDDM, a simplified model of the discovered dynamics, can well capture the widespread observation of smoothly curved trial-averaged trajectories.

bioRxiv preprint doi: https://doi.org/10.1101/2023.10.15.562427; this version posted November 20, 2023. The copyright holder for this preprint (which was not certified by peer review) is the author/funder. All rights reserved. No reuse allowed without permission.

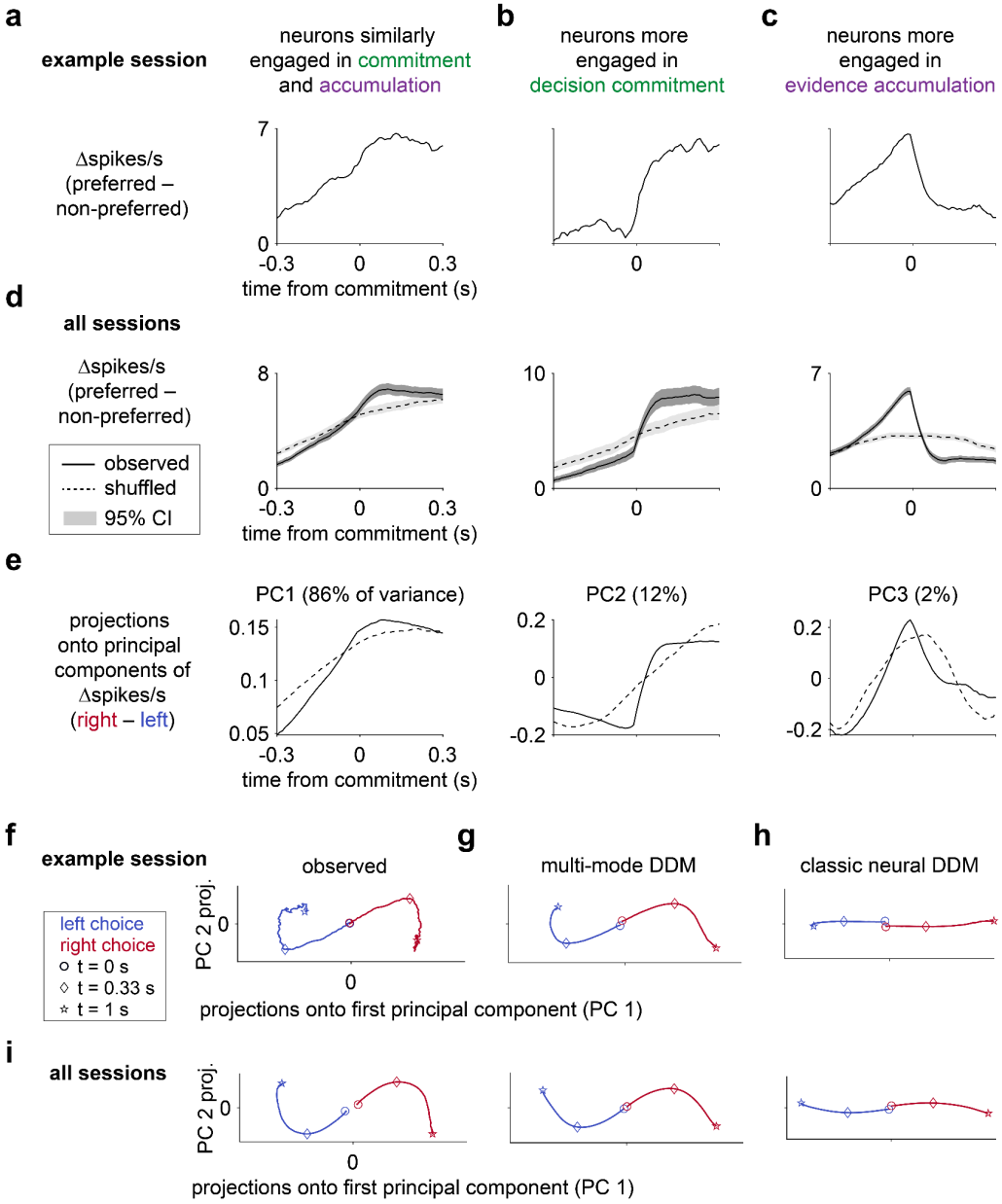

Figure 4. MMDDM captures ramping and stepping profiles and trial-averaged curved trajectories. **a**, The peri-commitment time histogram (PCTH) averaged across neurons that are similarly engaged in decision commitment and evidence accumulation show a ramp-to-bound profile. “Preferred” refers to the behavioral choice for which a neuron emitted more spikes. Example session. N=23 neurons. **b**, In the same session, the PCTH averaged across 10 neurons that are more strongly engaged in commitment has an abrupt, step-like profile. **c**, The ramp-and-decline profile characterizes the PCTH averaged across the 43 neurons from the same session that are more strongly engaged in evidence accumulation. **d**, Across sessions, the ramp-to-bound, step-like, and ramp-and-decline profile characterize the PCTH of neurons similarly engaged in commitment and accumulation (1,116), more engaged in commitment (414), and more engaged in accumulation (1,529), respectively. **e**, The ramp-to-bound, step-like, and ramp-and-decline profile are observed in the first three principal components of the PCTH’s. **f**, Curved trial-averaged trajectories. **g**, Out-of-sample predictions of the MMDDM. **h**, Out-of-sample predictions of the classic neural DDM fail to account the trial-averaged trajectories. **i**, Results are similar when neurons are pooled across sessions.

bioRxiv preprint doi: https://doi.org/10.1101/2023.10.15.562427; this version posted November 20, 2023. The copyright holder for this preprint (which was not certified by peer review) is the author/funder. All rights reserved. No reuse allowed without permission.

A gradient across brain regions in the strength of neural mode transitions

We observed dynamics with a neural mode transition across the multiple frontal cortical and striatal areas that we recorded: The (cross-validated) MMDDM better captures neural responses in each brain region than the classic neural DDM, than a bistable attractor model, and also a leaky accumulator model (**Fig**. 5a; Extended Data Fig. 12a-c). Other signatures of dynamics observed here, including peri-commitment neural changes (Extended Data Fig. 10a) and curved trial-averaged responses (Extended Data Fig. 11a) can be observed within each brain region. These results indicate that the dynamics observed here generalize across frontal cortex and striatum.

Nonetheless, quantitative differences can be observed across brain regions. The choice selectivity (a measure, ranging from -1 to 1, of the difference in firing rates for right versus left choice trials; Extended Data Fig. 8i) averaged across neurons shows different temporal profiles across brain regions (**Fig**. 5b). Whereas mPFC neurons are most choice-selective near the beginning, FOF neurons are most choice-selective toward the end. Focusing on the latency to the peak of the temporal profiles, the latency is the shortest for mPFC and the longest for FOF. This difference in the latency to peak across brain regions can be explained in the context of separate neural modes for evidence accumulation and decision commitment: neurons that are more strongly engaged in evidence accumulation ($w_{EA} > w_{DC}$) have a shorter latency to peak selectivity than neurons that are more strongly engaged in decision commitment ($w_{DC} > w_{EA}$). The latencies to peak choice selectivity suggest these frontal brain regions may differ in their relative engagement in evidence accumulation and decision commitment.

To test this possibility, we examined the encoding weights in MMDDM. For each neuron, we computed a scalar index that compares its relative engagement in the two processes, by taking the difference between the absolute values of the w_{EA} and w_{DC} and normalizing by the sum (**Fig**. 5c). A neuron with an index near 1 is engaged only in evidence accumulation (and shows a decay), whereas a neuron with an index near -1 is engaged only in decision commitment (and exhibits a delay). A neuron with a classic ramp profile must have an index near zero, which corresponds to equal levels of engagement. The distribution of the indices was unimodal, indicating the engagement in accumulation and commitment is distributed rather than clustered among neurons (Extended Data Fig. 12d-e). The engagement indices show that brain regions differ in their relative engagement in evidence accumulation: mPFC, dmFC, and dStr are more strongly engaged in evidence accumulation than the regions vStr, M1, and FOF. The rank order of the brain regions by the engagement index is similar to the rank order by time to peak latency. This result indicates that differences in choice-related encoding across frontal cortical and striatal regions can be understood in terms of relative participation in evidence accumulation versus decision commitment.

bioRxiv preprint doi: https://doi.org/10.1101/2023.10.15.562427; this version posted November 20, 2023. The copyright holder for this preprint (which was not certified by peer review) is the author/funder. All rights reserved. No reuse allowed without permission.

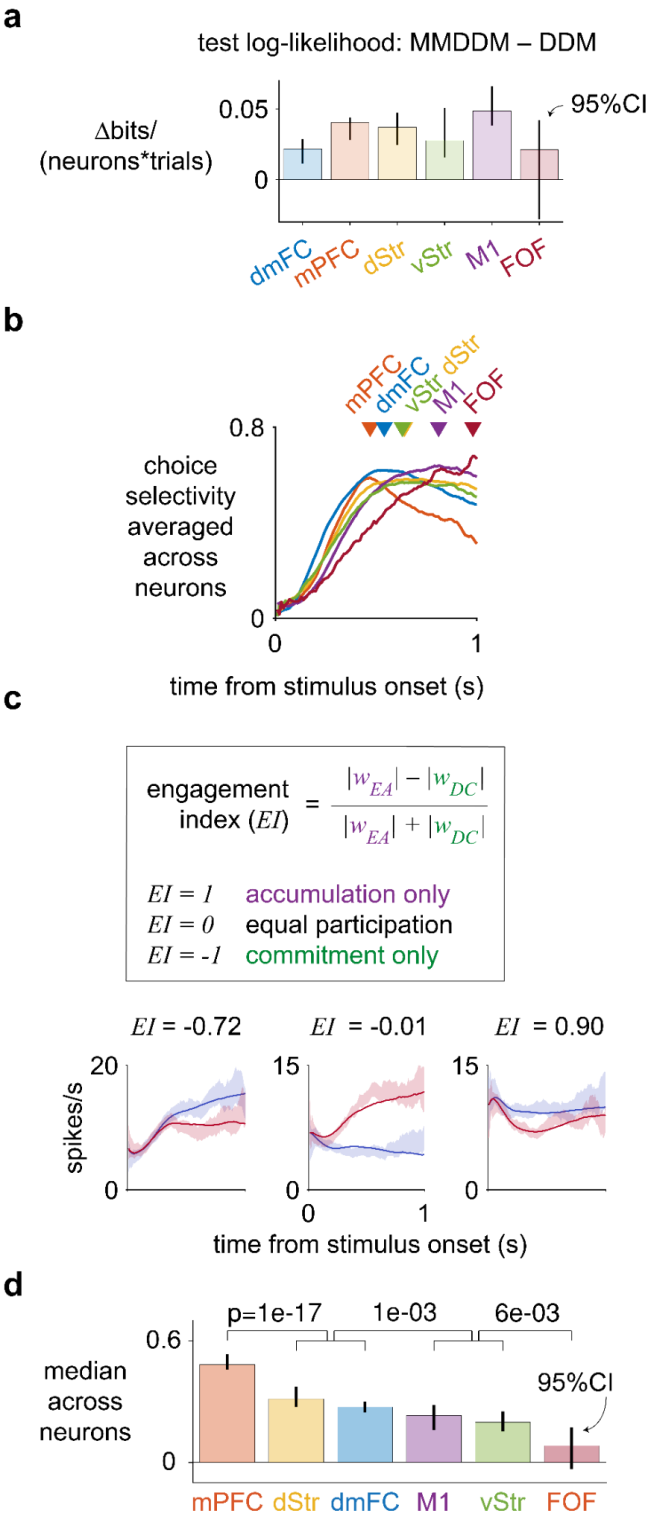

Figure 5. A gradient across brain regions in the strength of neural mode transitions. **a**, MMDDM better captures the data than the classic neural DDM. Error bar indicates 95% bootstrapped confidence intervals across sessions. N =29 dmFC sessions, 29 mPFC, 86 dStr, 74 vStr, 75 M1, and 7 FOF. **b**, The neuron-averaged choice selectivity has different temporal profiles across brain regions: mPFC neurons are most choice-selective near the beginning, while FOF neurons are most choice-selective toward the end. **c**, Using fits from MMDDM, a scalar index quantifies each neuron's relative level of engagement between evidence accumulation and decision commitment. **d**, A gradient of relative engagement in evidence accumulation and decision commitment across frontal brain regions. The rank order of the median engagement index well matches the rank of the latency to peak choice selectivity. Error bar indicates 95% bootstrapped confidence intervals across neurons.

Discussion

How attractor dynamics govern the formation of a perceptual choice has been long debated[1,6,9]. Here we suggest that attractor states play a major role only after the dynamics transition from a regime that is strongly driven by inputs to one dominated by the intrinsic dynamics. The initial input-driven regime mediates evidence accumulation, and the subsequent intrinsic-dominant regime subserves decision commitment. This regime transition is coupled to a rapid change in the representation of the decision process by the neural population. The neural mode (i.e., direction in neural space) representing evidence accumulation is almost orthogonal to the dimension representing decision commitment.

While the behavioral DDM is widely used, other frameworks are also prevalent, such as the linear ballistic accumulator[57] or urgency gating[58]. It is notable that the dynamics inferred by FINDR, obtained in a data-driven, unsupervised manner from spike times and auditory click times alone, resulted in regimes that match the characteristics of the behavioral DDM, but not of the alternatives. This match led us to explore a simplified model, the MMDDM, in which a scalar latent decision variable evolves as in the DDM, but is represented in different neural modes before versus after decision-commitment. We found this to provide a parsimonious explanation of a variety of experimental findings from multiple species: across primates and rodents, sensory inputs and choice are represented in separate neural dimensions[6–8,53,59,60] across time, and neither sensory

bioRxiv preprint doi: https://doi.org/10.1101/2023.10.15.562427; this version posted November 20, 2023. The copyright holder for this preprint (which was not certified by peer review) is the author/funder. All rights reserved. No reuse allowed without permission.

responses nor the neural dimensions for optimal decoding of the choice are fixed[7,59,60]. These phenomena, along with other observations including diversity in single neuron dynamics[50,51], curved average trajectories[7,8,53], choice behavior[36], and some vigorously debated phenomena such as a variety of single-neuron ramping versus stepping temporal profiles[4,5,61], are all captured by the MMDDM.

How do decisions end? In many studies, an animal is trained extensively to couple the termination of their deliberation with the initiation of a motor response. The motivation is to use the moment the animal initiates its response to operationally define when it commits to a choice[62,63]. Under this definition, neural activity before the movement is interpreted to correspond to deliberation per sé, with minimal contamination of post-commitment signals. Yet, committing to a choice and initiating a response are distinct processes[64], and many-month training may conflate neural activity underlying decision commitment and response preparation[65]. Here we show that the precise time of decision commitment on individual trials can be inferred without training an animal to couple their decision commitment to movement initiation. The peri-commitment neural responses observed here contrast sharply with the ramp-and-burst neural responses observed in animals trained to couple their decision commitment with response initiation[63]. The distinction between perceptual decision and movement preparation, and their interaction[66,67], may be addressed in future studies using dynamics inferred from both neural activity and the animal's pose.

Current proposals for implementing a DDM-like decision process in neural population dynamics have posited a one-dimensional manifold of slow intrinsic dynamics, along which evidence accumulation evolves, and towards which other states are attracted[1,35]. In contrast, the FINDR-inferred dynamics suggest an initial *two*-dimensional manifold of slow intrinsic dynamics. Sensory evidence inputs drive evidence accumulation along one of these slow dimensions. The other slow dimension corresponds to the decision commitment axis, along which intrinsic dynamics will become dominant later in the process. During the initial evidence accumulation, why would there be slow intrinsic dynamics along this second dimension? It is well known that during perceptual decision-making, non-sensory factors such as which choice option was rewarded on the previous trial[68–70] have a significant effect on subjects' choices. But the neural mechanisms for how such other factors and sensory evidence interact to produce the subject's final choice remain unclear. We speculate that the slow intrinsic dynamics along the decision commitment axis provide a mechanism for inputs driven by these other factors to influence choice, in a manner that is orthogonal and independent of the evolving representation of the accumulating evidence.

Finally, our approach expands the classic repertoire of techniques used to study perceptual decision-making. We inferred the decision dynamics directly from neural data rather than assuming a specific hypothesis, and we took steps to enhance the human-interpretability of the discovered dynamics: the unsupervised method (FINDR) focuses on low- rather than high-dimensional decision dynamics, and the mapping from latent to neural space (before each neurons' activation function) preserves angles and distances. Based on key features of the inferred latent dynamics, we developed a highly simplified, tractable model (MMDDM) that is directly relatable to a well-known framework. We found that the MMDDM, despite its simplicity, was able to describe a broad variety of previously-observed phenomena, and allowed us to infer the subject's internal decision commitment times on each trial. Pairing deep learning-based unsupervised discovery with simplified, parsimonious models may be a promising approach for studying not only perceptual decision-making but also other complex phenomena.

bioRxiv preprint doi: https://doi.org/10.1101/2023.10.15.562427; this version posted November 20, 2023. The copyright holder for this preprint (which was not certified by peer review) is the author/funder. All rights reserved. No reuse allowed without permission.

Extended Data Figures

Extended Data Figure 1

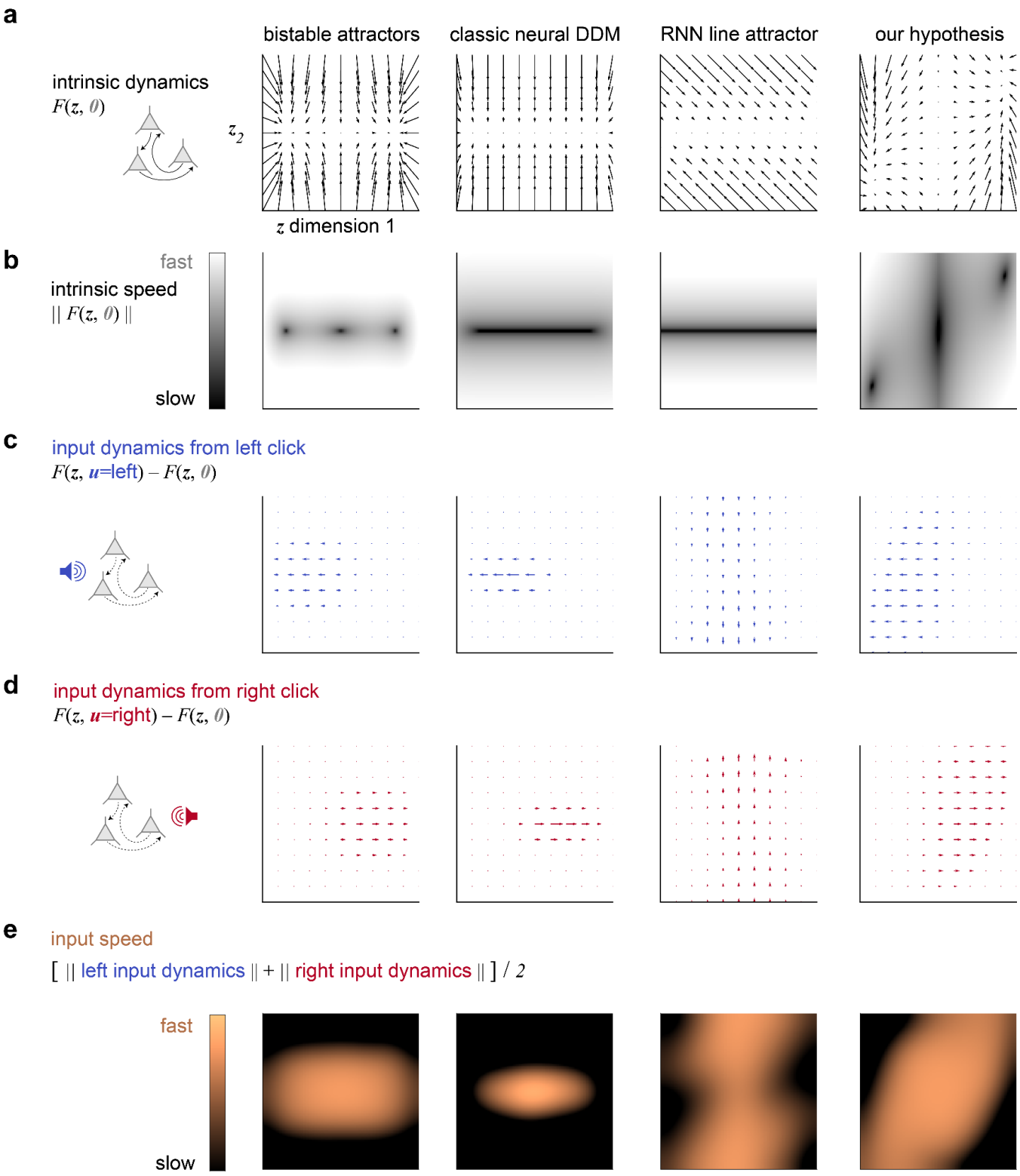

Extended Data Figure 1. Attractor hypotheses of perceptual decision-making. In these hypotheses, the decision process is represented by the state of a dynamical system, which we refer to as the “decision variable

bioRxiv preprint doi: https://doi.org/10.1101/2023.10.15.562427; this version posted November 20, 2023. The copyright holder for this preprint (which was not certified by peer review) is the author/funder. All rights reserved. No reuse allowed without permission.

(z)" and is depicted as two-dimensional here but may have fewer or more dimensions. An attractor is a set of states for which the dynamical system tends to move toward, from a variety of starting states. When z is in an attractor state, small perturbations away from the attractor tend to return the system toward the attractor. An attractor can implement the commitment to a choice and the maintenance of the choice in working memory. **a**, In all these hypotheses, the attractors are implemented by the intrinsic dynamics, which corresponds to the deterministic dynamics F in the absence of inputs and depends only on z itself. In the bistable attractors hypothesis, there are two discrete attractors, each of which corresponds to a choice alternative. In the classic neural DDM, the intrinsic dynamics form not only two discrete attractors but also a line attractor in between. The intervening line attractor allows an analog memory of the accumulated evidence when noise is relatively small. In the RNN line attractor hypothesis, the intrinsic dynamics form a line attractor, and a separate readout mechanism is necessary for the commitment to a discrete choice. Finally, in the dynamics discovered through unsupervised inference, the intrinsic dynamics form two discrete attractors. **b**, The intrinsic speed is the magnitude of the intrinsic dynamics. A dark region corresponds to a steady state, which can be an attractor, repeller, or saddle point. In the bistable attractors hypothesis, the left and right steady states are each centered on an attractor, and the middle is a saddle point. In both the classic neural DDM and the RNN line attractor hypothesis, the steady states correspond to attractors. Finally, in the dynamics observed through unsupervised inference, the left and right steady states are attractors, and the middle a repeller. **c-d**, Input dynamics corresponding to a left and right auditory pulse, respectively. Here we show the "effective" input dynamics, which is multiplied by the frequency $p(\boldsymbol{u}|z)$ to account for the pulsatile nature and the statistics of the stimuli in our task (in contrast to **Fig.** 1e, in which the input dynamics were presented without the multiplication of the frequency, which is appropriate for stimuli that are continuous over time, such as the random dot motion patches[46]). Whereas in the bistable attractor and classic neural DDM, the inputs are aligned to the attractors, in the RNN line attractor and discovered dynamics, the inputs are not aligned. **e**, The input speed is the average of the magnitude of the left input dynamics and the magnitude of the right input dynamics.

bioRxiv preprint doi: https://doi.org/10.1101/2023.10.15.562427; this version posted November 20, 2023. The copyright holder for this preprint (which was not certified by peer review) is the author/funder. All rights reserved. No reuse allowed without permission.

Extended Data Figure 2

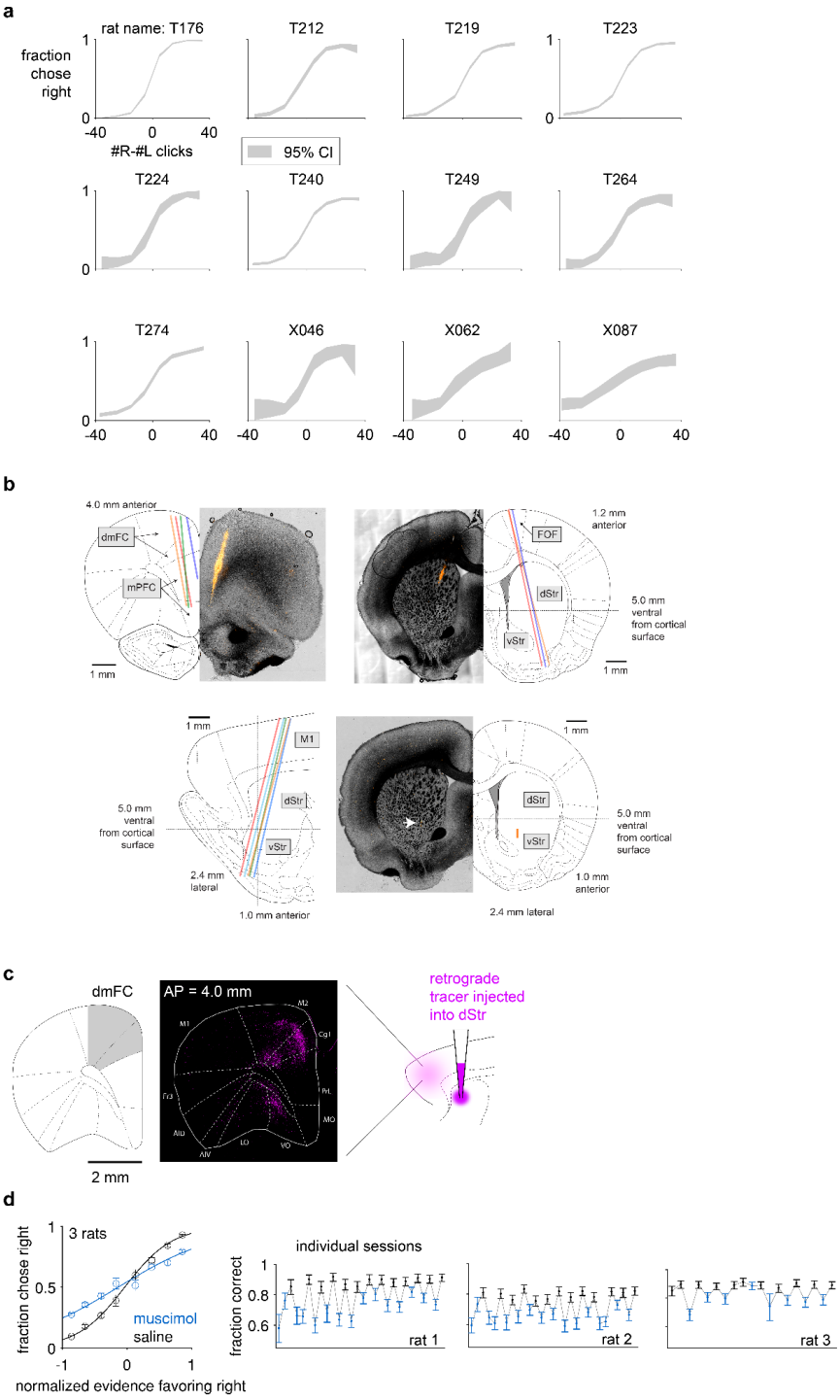

Extended Data Figure 2. Behavioral performance, histological slices, anatomical tracing, and the causal necessity of dmFC. **a**, Psychometric functions of each of the twelve rats recorded aggregated across recording sessions. **b**, Histological images of probe tracks. Each color indicates a probe chronically implanted in a rat. **c**, Dorsomedial frontal cortex (dmFC) provides a major input to the anterior dorsal striatum (dStr). **d**, dmFC is causally necessary for the auditory decision-making task studied here.

bioRxiv preprint doi: https://doi.org/10.1101/2023.10.15.562427; this version posted November 20, 2023. The copyright holder for this preprint (which was not certified by peer review) is the author/funder. All rights reserved. No reuse allowed without permission.

Extended Data Figure 3

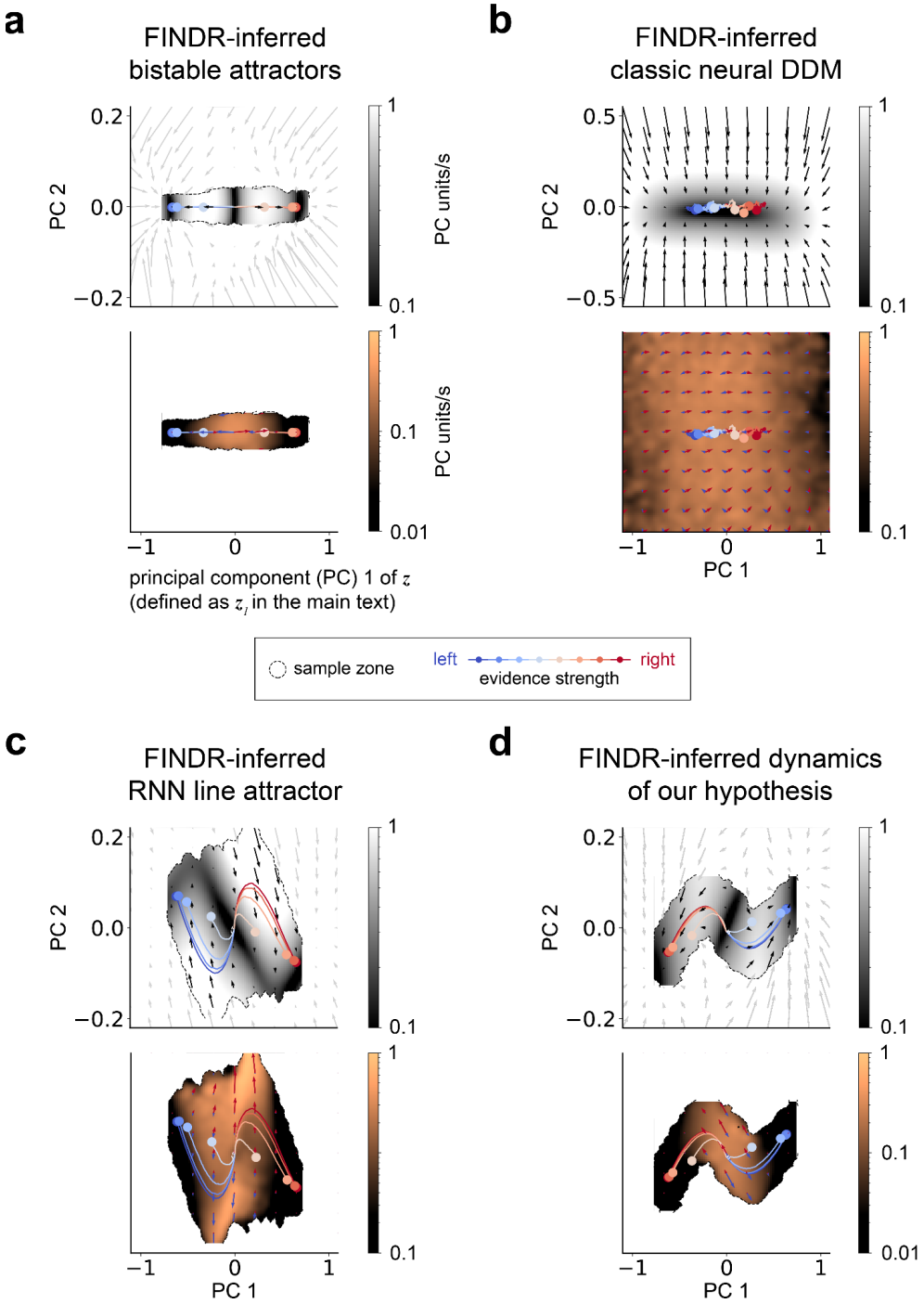

Extended Data Figure 3. FINDR can be used to distinguish between the dynamical systems hypotheses of perceptual decision-making. **a**, We simulated spikes that follow the bistable attractor dynamics in Extended Data Fig. 1 to create a synthetic dataset with the number of trials, number of neurons, and firing rates that are typical of the values observed in our datasets. Then, we fit FINDR to this synthetic dataset from random initial parameters. The intrinsic and input dynamics inferred by FINDR qualitatively match the bistable attractors hypothesis. **b-d**, FINDR-inferred dynamics qualitatively match the dynamics in **Fig**. 1g-i and Extended Data Fig. 1.

bioRxiv preprint doi: https://doi.org/10.1101/2023.10.15.562427; this version posted November 20, 2023. The copyright holder for this preprint (which was not certified by peer review) is the author/funder. All rights reserved. No reuse allowed without permission.

Extended Data Figure 4

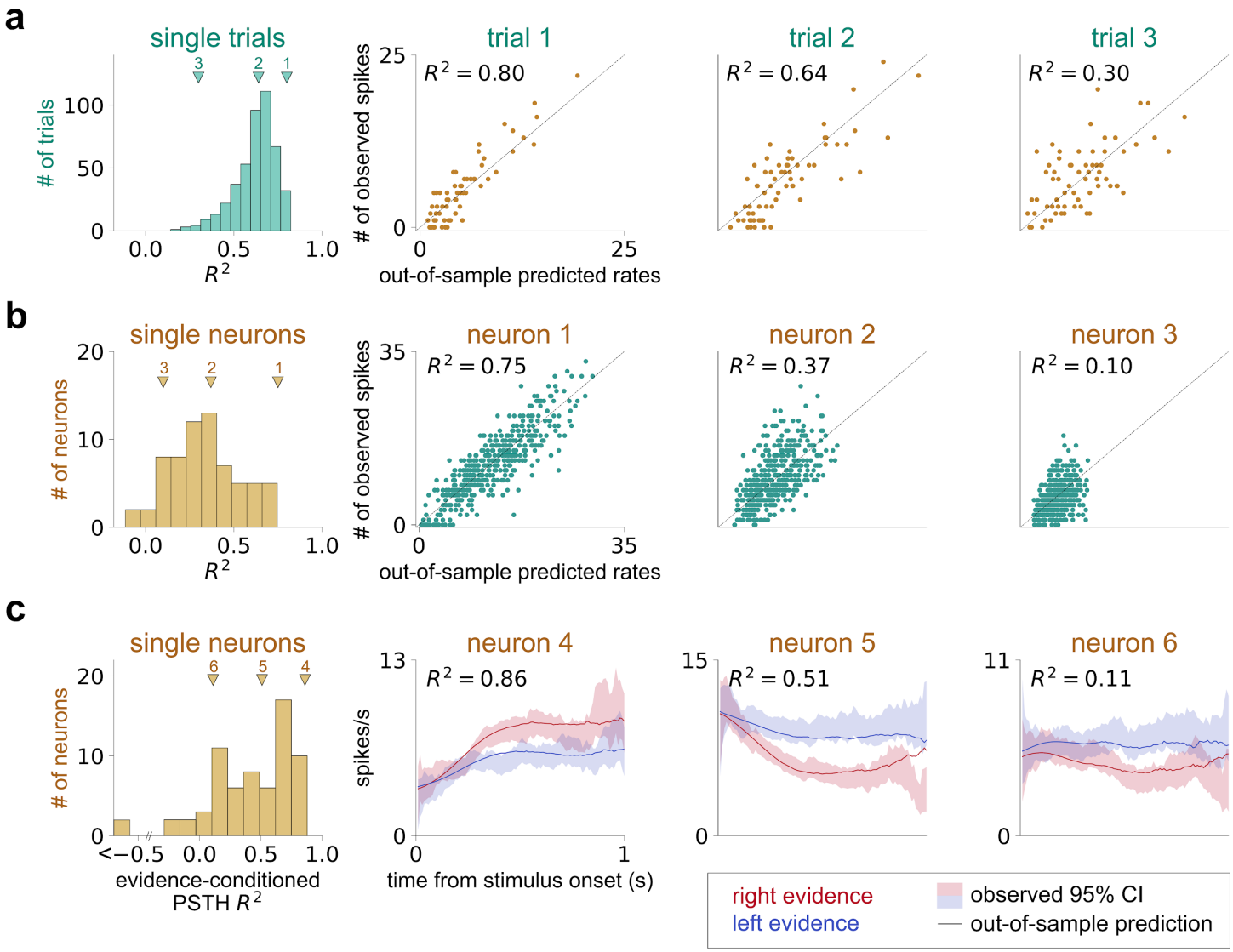

Extended Data Figure 4. FINDR can well capture the neural responses. **a-b**, FINDR captures the underlying firing rates of the single-trial responses of individual neurons from mPFC and dmFC from a representative session. **c**, FINDR captures the complex trial-averaged dynamics of individual neurons in mPFC and dmFC as can be seen in the peristimulus time histograms (PSTH). The goodness-of-fit is measured using the coefficient of determination (R^2).

bioRxiv preprint doi: https://doi.org/10.1101/2023.10.15.562427; this version posted November 20, 2023. The copyright holder for this preprint (which was not certified by peer review) is the author/funder. All rights reserved. No reuse allowed without permission.

Extended Data Figure 5

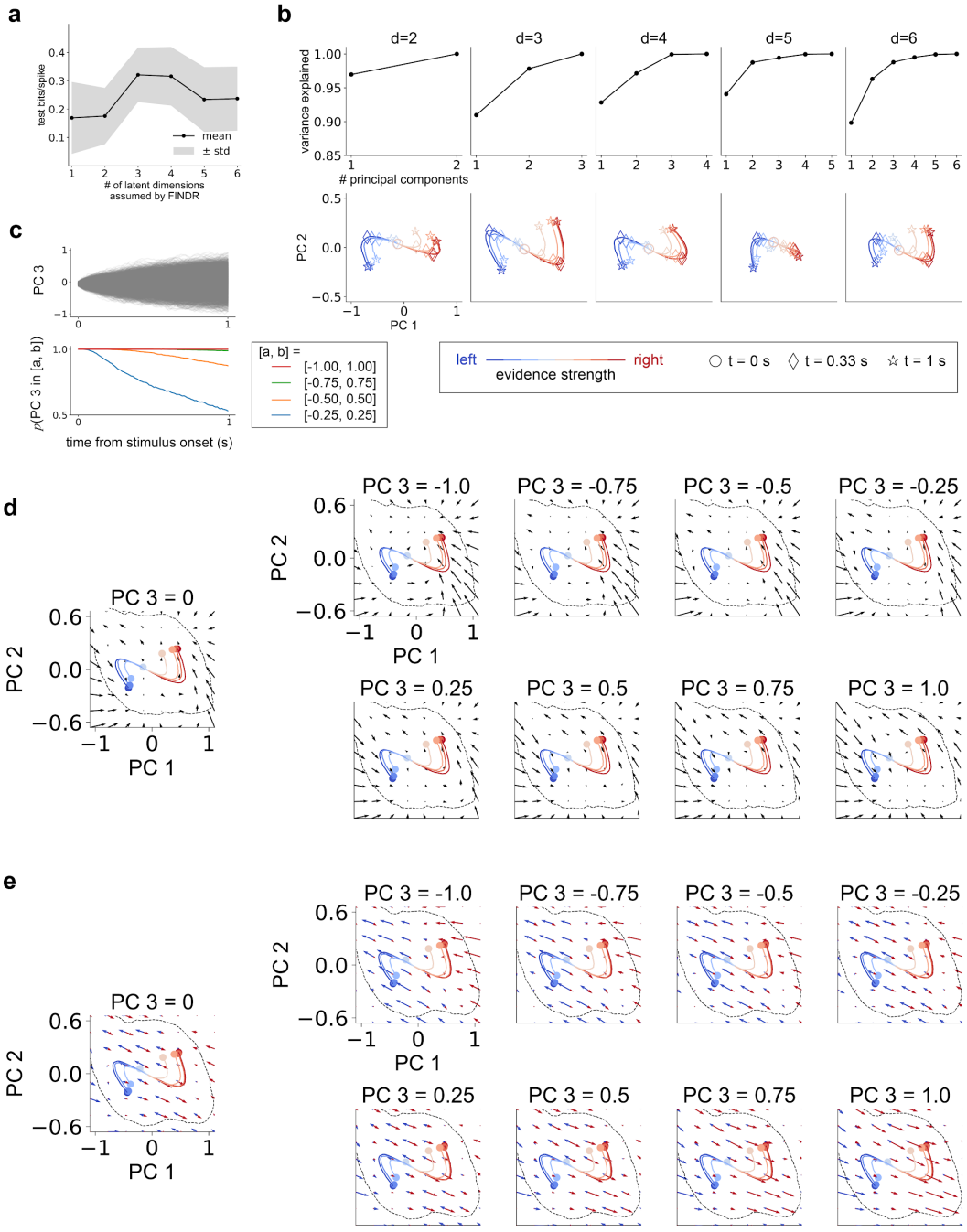

Extended Data Figure 5. FINDR reveals 2-dimensional decision-making dynamics. **a**, Across different FINDR models with dimensions (d) ranging from 1 to 6, the bits/spike of held-out trials maximizes for d=3. Trials were partitioned into 5 folds, and the standard deviation was computed across the 5 partitions. **b**, For FINDR models with different latent dimensions, more than 95% of the variance is captured by the first two principal components (PC's) for d=3-6. For models with two or more dimensions, the trajectories projected onto the first two dimensions were qualitatively similar. **c**, For the FINDR model with d=3, PC 3 takes a value between -0.25 and 0.25 for more than 50% of the trials, and does not go beyond -1 or 1. **d-e**, For the FINDR model with d=3, when we project intrinsic (**d**) and input (**e**) vector fields onto the first two PCs, the projected 2-d vector fields are similar across different PC 3 values. We show the vector fields with PC 3 = 0 in **Fig**. 2. Inside the dashed lines indicate the well-sampled subregion of the state space (sample zone).

bioRxiv preprint doi: https://doi.org/10.1101/2023.10.15.562427; this version posted November 20, 2023. The copyright holder for this preprint (which was not certified by peer review) is the author/funder. All rights reserved. No reuse allowed without permission.

Extended Data Figure 6

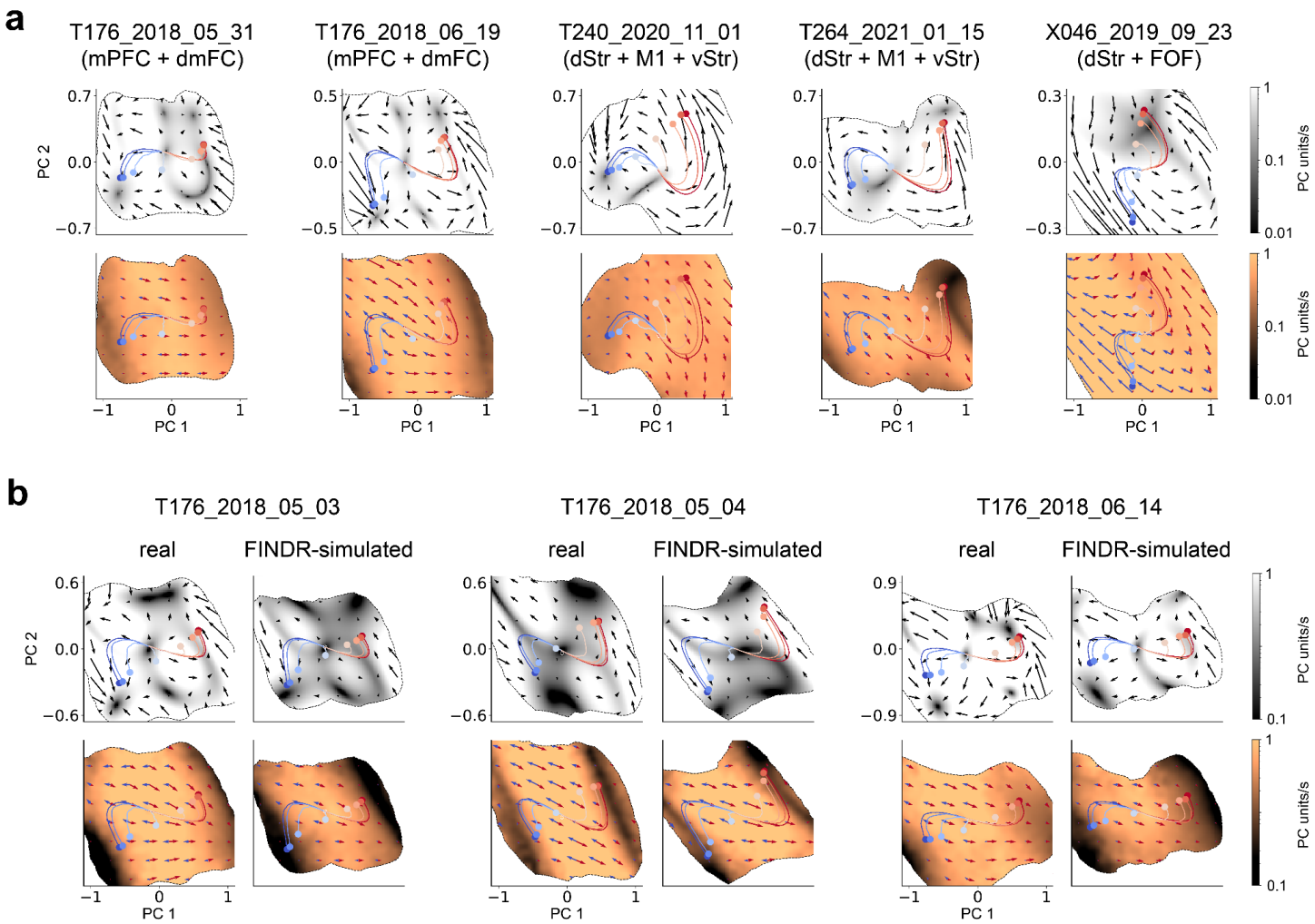

Extended Data Figure 6. Unsupervised inference of the dynamics across sessions, animals, and frontal brain regions. **a**, Non-aligned input and intrinsic dynamics across different recording sessions, animals, and brain regions. **b**, FINDR can reliably recover the inferred input and intrinsic dynamics. After fitting FINDR to a dataset, the model parameters are used to simulate a synthetic dataset using the exact same set of sensory stimuli in the real dataset and containing the same number of neurons and trials. From new initial parameter values, FINDR was fit to the simulated data to infer the “FINDR-simulated” vector fields.

bioRxiv preprint doi: https://doi.org/10.1101/2023.10.15.562427; this version posted November 20, 2023. The copyright holder for this preprint (which was not certified by peer review) is the author/funder. All rights reserved. No reuse allowed without permission.

Extended Data Figure 7

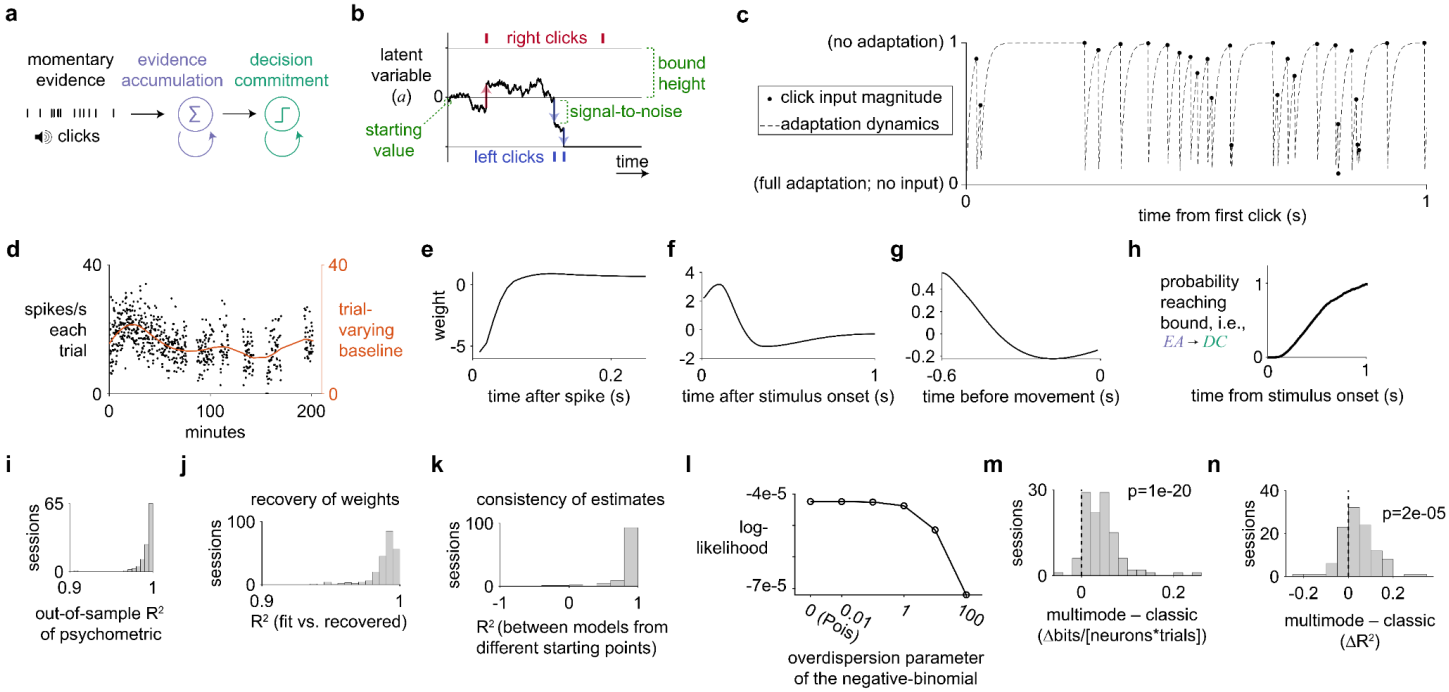

Extended Data Figure 7. Multi-mode drift-diffusion model (MMDDM). **a**, The discovered motifs are consistent with two-stage, sequential processing: momentary evidence is first accumulated over time until a fixed threshold is reached, at which point decision commitment occurs and the choice is maintained in memory. **b**, The three parameters that are fit in MMDDM consist of the bound height, the starting value, and the signal-to-noise of each momentary input. **c**, The magnitude of the input after sensory adaptation of each click in a simulated Poisson auditory click train. Based on previous findings[36], the adaptation strength (φ) is fixed to 0.001, and the post-adaptation recovery rate (k) to 100. The generative click rate is 40 hz, as in the behavioral task. **d**, The slowly trial-varying baseline function, parametrized by smooth temporal basis functions, for an example neuron. The baseline is added before the softplus nonlinearity. **e**, The spike history filter of the same neuron. **f**, The post-stimulus filter of the neuron. This filter does not depend on the content of the click train and only depends on the timing of the first click. **g**, The kernel of the same neuron to account for movement anticipation. The kernel does not depend on the actual choice of the animal. **h**, The cumulative probability of the latent variable reaching decision commitment over time in a simulated trial. **i**, The psychometric function is well captured across sessions. **j**, After fitting the model to each recording session, the learned parameters are used to simulate a data set, using the same number of trials and the same auditory click trains. The simulations are used to fit a new model, the recovery model, starting from randomized parameter values. The encoding weights of the accumulated evidence of the recovery model are compared against the weights used for the simulation (which were learned by fitting to the data) using the coefficient-of-determination metric. **k**, Consistency in the encoding weights between the training models during five-fold cross-validation. For each session, a coefficient-of-determination was computed for each pair of training models (10 pairs), and the median is included in the histogram. **l**, Whereas the Poisson distribution requires the mean to be the same as the variance, the negative binomial distribution is a count response model that allows the variance to be larger than the mean μ, with an additional parameter α, the overdispersion parameter, that specifies the variance to be equal to $\mu+\alpha\mu^2$. When the overdispersion parameter is zero, the distribution is equivalent to a Poisson. Fitting the data to varying values of the overdispersion parameter shows that log-likelihood is maximized with a Poisson distribution for the conditional spike count response. Similarly when the overdispersion parameter was learned from the data, the best fit values were all close to zero. **m**, Sensory adaptation is not critical to the

bioRxiv preprint doi: https://doi.org/10.1101/2023.10.15.562427; this version posted November 20, 2023. The copyright holder for this preprint (which was not certified by peer review) is the author/funder. All rights reserved. No reuse allowed without permission.

improvement in fit by by the MMDDM compared to the classic neural DDM. Even without modeling sensory adaptation–by setting φ=1 and k=0, such that every click has the same input magnitude–the out-of-sample log-likelihood is reliably improved by the MMDDM compared to the classic neural DDM. **n**, The out-of-sample goodness-of-fit of the PSTH's is also reliably improved even in the absence of sensory adaptation.

bioRxiv preprint doi: https://doi.org/10.1101/2023.10.15.562427; this version posted November 20, 2023. The copyright holder for this preprint (which was not certified by peer review) is the author/funder. All rights reserved. No reuse allowed without permission.

Extended Data Figure 8

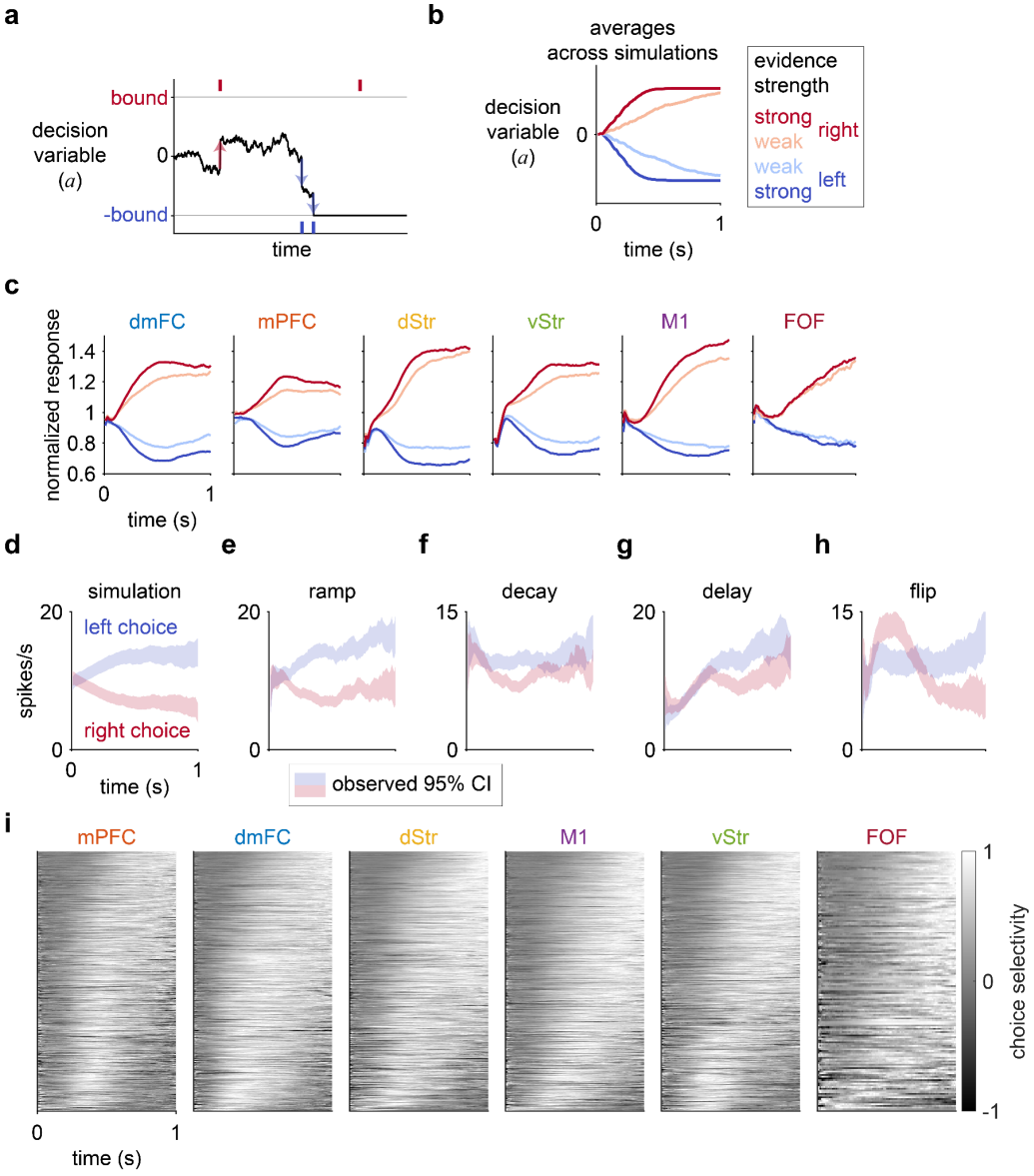

Extended Data Figure 8. The temporal profiles of the choice selectivity of individual neurons are heterogeneous, and this diversity is not consistent with an one-dimensional neural representation of the decision variable in the behavioral drift-diffusion model (DDM). **a**, The behavioral DDM hypothesizes that noisy inputs are accumulated over time through a one-dimensional decision variable (a) until the value of a reaches a fixed bound, which triggers the commitment to a choice. **b**, In simulations of the behavioral DDM, a ramps quickly when the evidence strength is strong and more slowly when the strength is weak. **c**, Responses averaged across both trials and neurons resemble the trajectories of a averaged across simulations. Only choice-selective neurons were included. Spikes after the animal began movement (i.e., removed its nose in the center port) were excluded. For this analysis only, error trials were excluded. N = 1324 (dmFC), 1076 (mPFC), 1289 (dStr), 714 (vStr), 822 (M1), 163 (FOF). **d**, The responses of a simulated neuron encoding the behavioral DDM shows the classic ramping dynamics. Shading indicates the bootstrapped 95% confidence interval of the trial-mean of the filtered response. **e**, A neuron with a classic ramp profile. **f**, A neuron recorded from the session with choice selectivity that decays over time. **g**, A neuron exhibiting a substantial delay in its choice selectivity. **h**, A neuron whose choice selectivity flips in sign. **i**, The diversity of the temporal profile of the choice selectivity of individual neurons are not consistent with a one-dimensional dynamical process.

bioRxiv preprint doi: https://doi.org/10.1101/2023.10.15.562427; this version posted November 20, 2023. The copyright holder for this preprint (which was not certified by peer review) is the author/funder. All rights reserved. No reuse allowed without permission.

Extended Data Figure 9

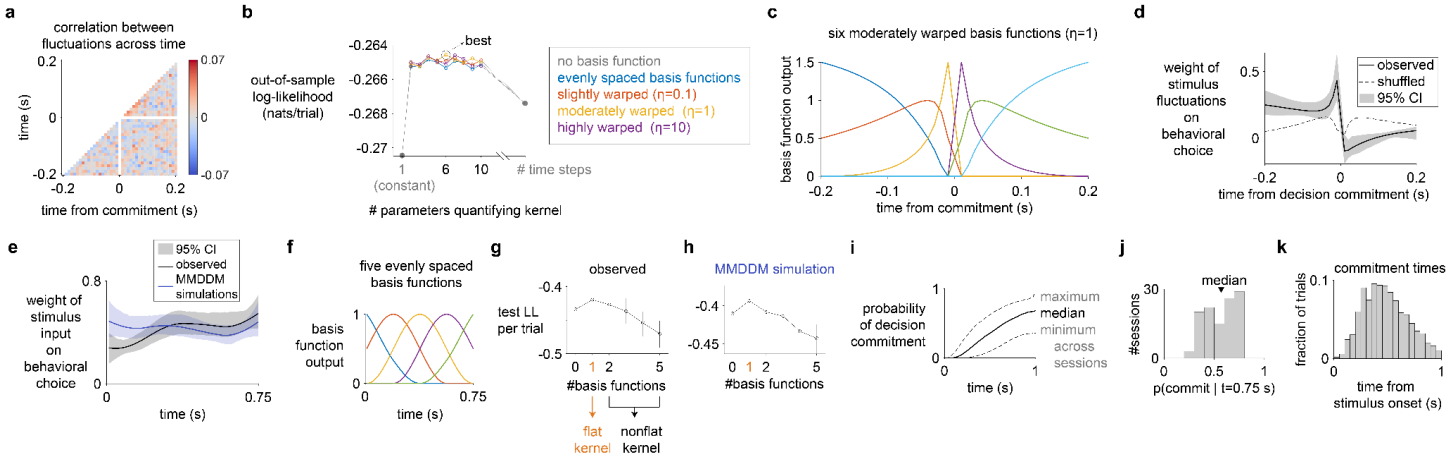

Extended Data Figure 9. The psychophysical kernel shown in **Fig.** 3m of the main text was estimated using time bins of 0.01 s, spanning +/-0.2 s around the decision commitment time. In this extended data figure we repeat the psychophysical kernel estimate, but using basis functions and cross-validation to select the basis functions that provide the optimal smoothing of the signal. The results shown here and shown in **Fig.** 3m of the main text are qualitatively similar and lead to the same conclusions. **a**, For the inferred weights of the stimulus fluctuations to be interpretable, the click input fluctuations must not be strongly correlated across time steps. On each time step on each trial, the fluctuation in auditory click input was computed by counting the observed difference in right and left clicks at that time step, and then subtracting from it the expected difference given the random processes used to generate the stimulus. The input fluctuations at time step of t=0 s were excluded because they are strongly correlated with the input fluctuations before decision commitment and strongly anti-correlated with input fluctuations after commitment. **b**, To determine the time resolution of the kernel that best captures the weight of the input fluctuations, 10-fold cross-validation was performed to compare kernels quantified by different numbers of parameters and types of basis functions. The kernel with the lowest temporal resolution is a constant, represented by a single parameter, implying that fluctuations across time have the same weight. At the highest time resolution, the kernel can be parametrized by a separate weight for each time step. At intermediate time resolution, the kernel is parametrized by basis functions that span the temporal window. The basis functions can be evenly spaced across the temporal window, or stretched such that time near t=0 s is represented with higher resolution and time far from t=0 s with lower resolution. The most likely model had six moderately stretched (η=1) basis functions. **c**, The optimal model's set of six moderately stretched (η=1) basis functions. **d**, Even when using basis functions, the psychophysical kernel is consistent with the core prediction of MMDDM: The psychophysical weight of the stimulus fluctuations on the behavioral choice ceases after the time of decision commitment. Note that no basis function was used in the analysis in **Fig.** 3m. **e**, In contrast to the commitment-aligned kernel, the kernel aligned to the onset of the auditory click trains is smooth. Mean stimulus onset-aligned psychophysical kernel across sessions, estimated using a model with five temporal basis functions. For each session, 10-fold cross-validation was performed on fitting the kernel model to the data, and ten estimated kernels are averaged. Then, the kernels are averaged across sessions. **f**, The onset-aligned psychophysical kernel is parametrized by five evenly spaced radial basis functions. **g**, Cross-validated model comparison shows that a temporally flat psychophysical kernel is most likely given the observed data. **h**, Similarly, given the simulated choices generated by the MMDDM, the out-of-sample log-likelihood is maximized by assuming a flat kernel. **i**, The approximately flat psychophysical kernel inferred from MMDDM-simulated choices is consistent with the MMDDM's prediction of the probability of decision commitment given the stimulus: throughout the trial, the probability of decision commitment is relatively low, and at no point in the trial is decision commitment an absolute certainty. **j**, At t=0.75 s, the

bioRxiv preprint doi: https://doi.org/10.1101/2023.10.15.562427; this version posted November 20, 2023. The copyright holder for this preprint (which was not certified by peer review) is the author/funder. All rights reserved. No reuse allowed without permission.

window used to compute the psychophysical kernel, the median probability of decision commitment across sessions is 0.57. **k,** Among the 34.7% of trials for which the commitment times could be inferred, the commitment times occur at variable times relative to time from stimulus onset. The fraction of trials declines for longer durations after stimulus onset because the stimulus duration on each trial is randomly drawn from 0.2-1.0 s.

bioRxiv preprint doi: https://doi.org/10.1101/2023.10.15.562427; this version posted November 20, 2023. The copyright holder for this preprint (which was not certified by peer review) is the author/funder. All rights reserved. No reuse allowed without permission.

Extended Data Figure 10

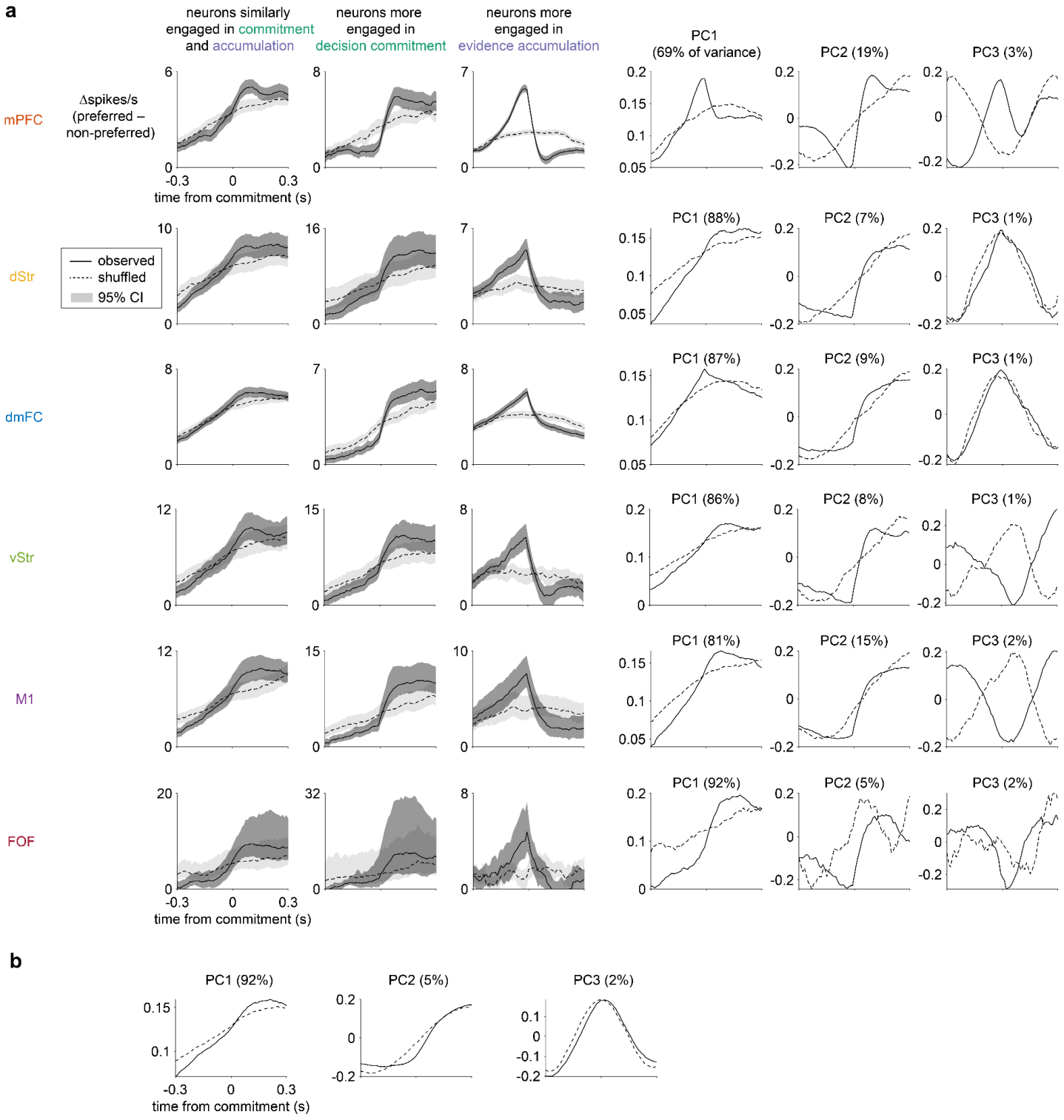

Extended Data Figure 10. The ramp-to-bound, step-like, and ramp-and-decline profiles can be observed in individual brain regions (panel **a**), and the ramp-to-bound, step-like profiles can be observed in neurons not choice-selective enough to be included in model analysis (panel **b**).

bioRxiv preprint doi: https://doi.org/10.1101/2023.10.15.562427; this version posted November 20, 2023. The copyright holder for this preprint (which was not certified by peer review) is the author/funder. All rights reserved. No reuse allowed without permission.

Extended Data Figure 11

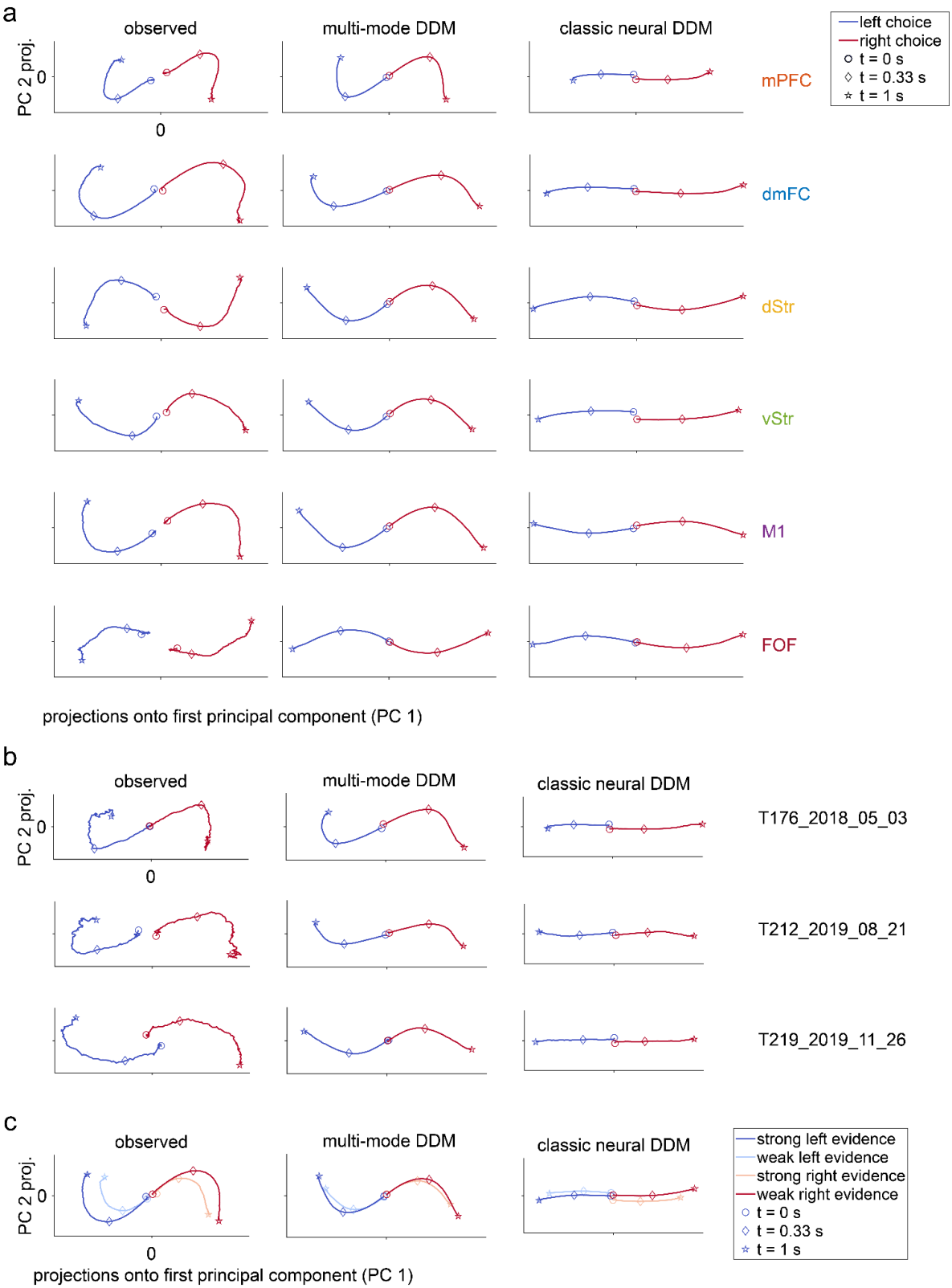

Extended Data Figure 11. The multi-mode drift-diffusion model (MMDDM) captures curved population trajectories when the analysis is performed on data from **a**, individual brain regions; **b**, individual sessions; and **c**, on trials conditions that depend on not only the choice but also the evidence.

bioRxiv preprint doi: https://doi.org/10.1101/2023.10.15.562427; this version posted November 20, 2023. The copyright holder for this preprint (which was not certified by peer review) is the author/funder. All rights reserved. No reuse allowed without permission.

Extended Data Figure 12

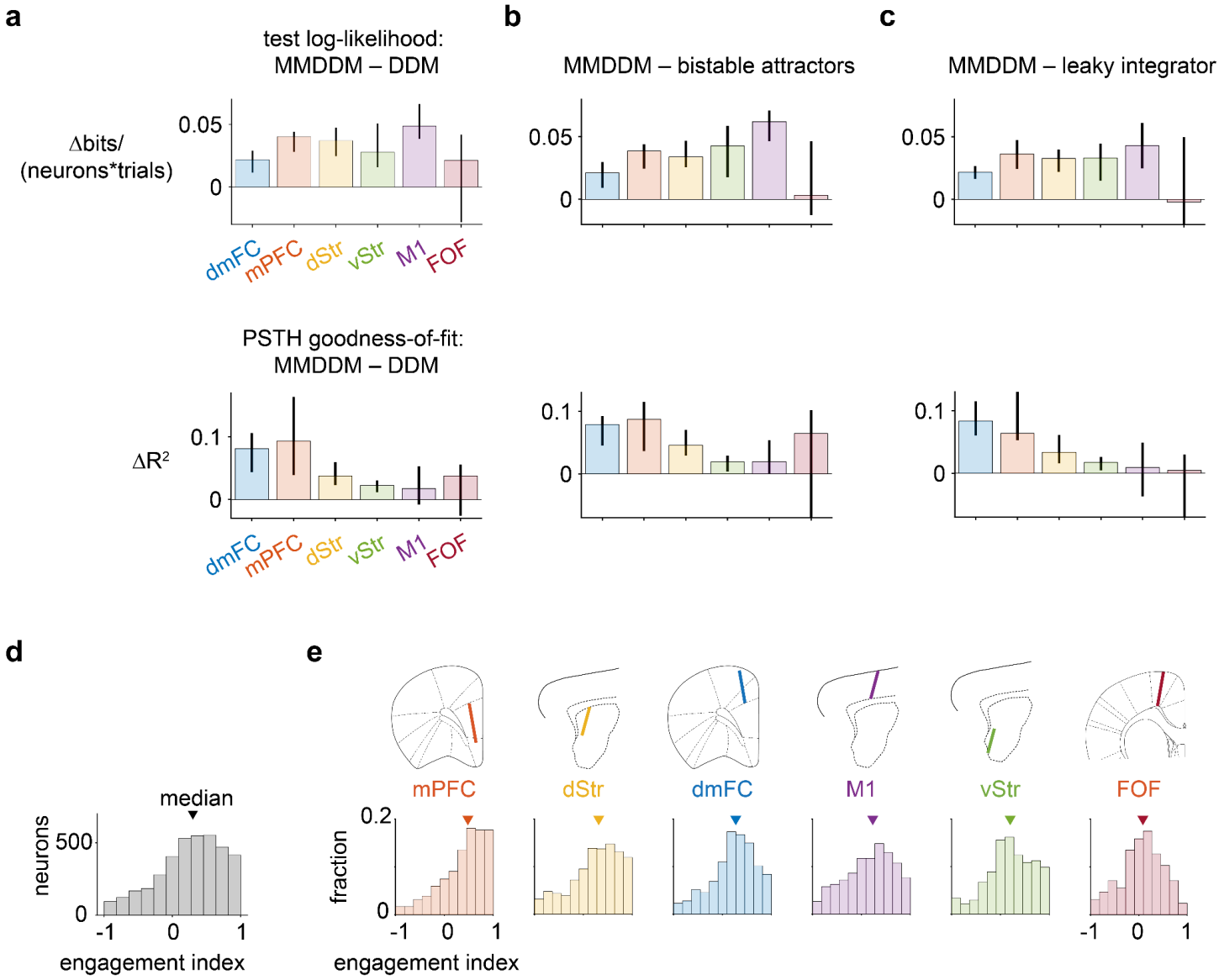

Extended Data Figure 12. Dynamics across brain regions. **a**, Top, comparison of the out-of-sample log-likelihood between the MMDDM and the classic neural DDM. Bottom, comparison of the out-of-sample R^2 of the PSTH across brain regions. Error bar indicates 95% bootstrapped confidence intervals across sessions. **b**, Comparison between MMDDM and bistable attractor model, which is implemented identically to the classic neural DDM except that the feedback parameter of the latent decision variable is not constrained to be zero but allowed to vary between 0 and 5 and is fit to the data. **c**, Comparison between MMDDM and bistable attractor model, which is implemented identically to the classic neural DDM except that the feedback parameter of the latent decision variable is not constrained to be zero but allowed to vary between 0 and -5 and is fit to the data. **d**, The median engagement index is not centered at zero, indicating that frontal cortical and striatal neurons are more strongly engaged in evidence accumulation than in decision commitment. **e**, The differences between the brain regions are apparent in their distribution: whereas the medial prefrontal cortex (mPFC)'s distribution is centered near 1, the distribution for frontal cortical orienting fields (FOF) neurons is centered at zero.

bioRxiv preprint doi: https://doi.org/10.1101/2023.10.15.562427; this version posted November 20, 2023. The copyright holder for this preprint (which was not certified by peer review) is the author/funder. All rights reserved. No reuse allowed without permission.

Author contributions

T.Z.L. and D.G. collected data. T.D.K. developed the FINDR model. T.Z.L. developed the MMDDM model. T.Z.L. and T.D.K. performed analyses. A.G.B. and C.D.K. assisted with data collection. V.A.E. and B.D. assisted with analyses. T.Z.L, T.D.K., and C.D.B. wrote the manuscript and conceptualized the study.

Acknowledgments

We thank Julie Charlton, Long Ding, Joshua Gold, Robbe Goris, John Maunsell, and Jonathan Pillow for their suggestions and comments. We also thank Jessica Morrison, Klaus Osario, Jovanna Teran, and Emily Valance for technical assistance. This work was supported by grants from NIH F32 MH115416 and NIH R01MH108358.

References

1. Wong, K.-F. & Wang, X.-J. A recurrent network mechanism of time integration in perceptual decisions. *J. Neurosci.* **26**, 1314–1328 (2006).
2. Dubreuil, A., Valente, A., Beiran, M., Mastrogiuseppe, F. & Ostojic, S. The role of population structure in computations through neural dynamics. *Nat. Neurosci.* **25**, 783–794 (2022).
3. Bollimunta, A., Totten, D. & Ditterich, J. Neural dynamics of choice: single-trial analysis of decision-related activity in parietal cortex. *J. Neurosci.* **32**, 12684–12701 (2012).
4. Latimer, K. W., Yates, J. L., Meister, M. L. R., Huk, A. C. & Pillow, J. W. NEURONAL MODELING. Single-trial spike trains in parietal cortex reveal discrete steps during decision-making. *Science* **349**, 184–187 (2015).
5. Zoltowski, D. M., Latimer, K. W., Yates, J. L., Huk, A. C. & Pillow, J. W. Discrete Stepping and Nonlinear Ramping Dynamics Underlie Spiking Responses of LIP Neurons during Decision-Making. *Neuron* **102**, 1249–1258.e10 (2019).
6. Mante, V., Sussillo, D., Shenoy, K. V. & Newsome, W. T. Context-dependent computation by recurrent dynamics in prefrontal cortex. *Nature* **503**, 78–84 (2013).
7. Aoi, M. C., Mante, V. & Pillow, J. W. Prefrontal cortex exhibits multidimensional dynamic encoding during decision-making. *Nat. Neurosci.* **23**, 1410–1420 (2020).
8. Yao, J. D. *et al.* Transformation of acoustic information to sensory decision variables in the parietal cortex. *Proc. Natl. Acad. Sci. U. S. A.* **120**, e2212120120 (2023).

bioRxiv preprint doi: https://doi.org/10.1101/2023.10.15.562427; this version posted November 20, 2023. The copyright holder for this preprint (which was not certified by peer review) is the author/funder. All rights reserved. No reuse allowed without permission.

9. Khona, M. & Fiete, I. R. Attractor and integrator networks in the brain. *Nat. Rev. Neurosci.* **23**, 744–766 (2022).
10. Inagaki, H. K., Fontolan, L., Romani, S. & Svoboda, K. Discrete attractor dynamics underlies persistent activity in the frontal cortex. *Nature* **566**, 212–217 (2019).
11. Gardner, R. J. *et al.* Toroidal topology of population activity in grid cells. *Nature* **602**, 123–128 (2022).
12. Sorscher, B., Mel, G. C., Ocko, S. A., Giocomo, L. M. & Ganguli, S. A unified theory for the computational and mechanistic origins of grid cells. *Neuron* **111**, 121–137.e13 (2023).
13. Briggman, K. L., Abarbanel, H. D. I. & Kristan, W. B., Jr. Optical imaging of neuronal populations during decision-making. *Science* **307**, 896–901 (2005).
14. Nieh, E. H. *et al.* Geometry of abstract learned knowledge in the hippocampus. *Nature* **595**, 80–84 (2021).
15. Churchland, M. M. *et al.* Neural population dynamics during reaching. *Nature* **487**, 51–56 (2012).
16. Kaufman, M. T., Churchland, M. M., Ryu, S. I. & Shenoy, K. V. Cortical activity in the null space: permitting preparation without movement. *Nat. Neurosci.* **17**, 440–448 (2014).
17. Chaudhuri, R., Gerçek, B., Pandey, B., Peyrache, A. & Fiete, I. The intrinsic attractor manifold and population dynamics of a canonical cognitive circuit across waking and sleep. *Nat. Neurosci.* **22**, 1512–1520 (2019).
18. Wang, X.-J. Decision making in recurrent neuronal circuits. *Neuron* **60**, 215–234 (2008).
19. Machens, C. K., Romo, R. & Brody, C. D. Flexible control of mutual inhibition: a neural model of two-interval discrimination. *Science* **307**, 1121–1124 (2005).
20. Wei, Z., Inagaki, H., Li, N., Svoboda, K. & Druckmann, S. An orderly single-trial organization of population dynamics in premotor cortex predicts behavioral variability. *Nat. Commun.* **10**, 216 (2019).
21. Genkin, M., Shenoy, K. V., Chandrasekaran, C. & Engel, T. A. The dynamics and geometry of choice in premotor cortex. *bioRxiv* 2023.07.22.550183 (2023) doi:10.1101/2023.07.22.550183.
22. Rajan, K., Harvey, C. D. & Tank, D. W. Recurrent Network Models of Sequence Generation and Memory. *Neuron* **90**, 128–142 (2016).
23. Prat-Ortega, G., Wimmer, K., Roxin, A. & de la Rocha, J. Flexible categorization in perceptual decision making. *Nat. Commun.* **12**, 1283 (2021).

bioRxiv preprint doi: https://doi.org/10.1101/2023.10.15.562427; this version posted November 20, 2023. The copyright holder for this preprint (which was not certified by peer review) is the author/funder. All rights reserved. No reuse allowed without permission.

24. Thura, D. & Cisek, P. Deliberation and commitment in the premotor and primary motor cortex during dynamic decision making. *Neuron* **81**, 1401–1416 (2014).
25. Mohan, K., Zhu, O. & Freedman, D. J. Interaction between neuronal encoding and population dynamics during categorization task switching in parietal cortex. *Neuron* **109**, 700–712.e4 (2021).
26. Galgali, A. R., Sahani, M. & Mante, V. Residual dynamics resolves recurrent contributions to neural computation. *Nat. Neurosci.* (2023) doi:10.1038/s41593-022-01230-2.
27. Finkelstein, A. *et al.* Attractor dynamics gate cortical information flow during decision-making. *Nat. Neurosci.* **24**, 843–850 (2021).
28. Wimmer, K., Nykamp, D. Q., Constantinidis, C. & Compte, A. Bump attractor dynamics in prefrontal cortex explains behavioral precision in spatial working memory. *Nat. Neurosci.* **17**, 431–439 (2014).
29. Pandarinath, C. *et al.* Inferring single-trial neural population dynamics using sequential auto-encoders. *Nat. Methods* **15**, 805–815 (2018).
30. Schneider, S., Lee, J. H. & Mathis, M. W. Learnable latent embeddings for joint behavioural and neural analysis. *Nature* **617**, 360–368 (2023).
31. Kim, T. D. *et al.* Flow-field inference from neural data using deep recurrent networks. *bioRxiv* (2023).
32. Ratcliff, R. & McKoon, G. The diffusion decision model: theory and data for two-choice decision tasks. *Neural Comput.* **20**, 873–922 (2008).
33. Vickers, D. Evidence for an accumulator model of psychophysical discrimination. *Ergonomics* **13**, 37–58 (1970).
34. Gold, J. I. & Shadlen, M. N. The neural basis of decision making. *Annu. Rev. Neurosci.* **30**, 535–574 (2007).
35. Bogacz, R., Brown, E., Moehlis, J., Holmes, P. & Cohen, J. D. The physics of optimal decision making: a formal analysis of models of performance in two-alternative forced-choice tasks. *Psychol. Rev.* **113**, 700–765 (2006).
36. Brunton, B. W., Botvinick, M. M. & Brody, C. D. Rats and humans can optimally accumulate evidence for decision-making. *Science* **340**, 95–98 (2013).
37. Hyafil, A. *et al.* Temporal integration is a robust feature of perceptual decisions. *Elife* **12**, (2023).

bioRxiv preprint doi: https://doi.org/10.1101/2023.10.15.562427; this version posted November 20, 2023. The copyright holder for this preprint (which was not certified by peer review) is the author/funder. All rights reserved. No reuse allowed without permission.

38. Erlich, J. C., Brunton, B. W., Duan, C. A., Hanks, T. D. & Brody, C. D. Distinct effects of prefrontal and parietal cortex inactivations on an accumulation of evidence task in the rat. *Elife* **4**, (2015).

39. Hanks, T. D. *et al.* Distinct relationships of parietal and prefrontal cortices to evidence accumulation. *Nature* **520**, 220–223 (2015).

40. Yartsev, M. M., Hanks, T. D., Yoon, A. M. & Brody, C. D. Causal contribution and dynamical encoding in the striatum during evidence accumulation. *Elife* **7**, (2018).

41. Hunnicutt, B. J. *et al.* A comprehensive excitatory input map of the striatum reveals novel functional organization. *Elife* **5**, (2016).

42. Anastasiades, P. G. & Carter, A. G. Circuit organization of the rodent medial prefrontal cortex. *Trends Neurosci.* (2021) doi:10.1016/j.tins.2021.03.006.

43. Sussillo, D., Jozefowicz, R., Abbott, L. F. & Pandarinath, C. LFADS - Latent Factor Analysis via Dynamical Systems. *arXiv [cs.LG]* (2016).

44. Keshtkaran, M. R. *et al.* A large-scale neural network training framework for generalized estimation of single-trial population dynamics. *Nat. Methods* **19**, 1572–1577 (2022).

45. Kim, T. D., Can, T. & Krishnamurthy, K. Trainability, Expressivity and Interpretability in Gated Neural ODEs. in *Proceedings of ICML* (2023).

46. Newsome, W. T., Britten, K. H. & Movshon, J. A. Neuronal correlates of a perceptual decision. *Nature* **341**, 52–54 (1989).

47. Kiani, R., Hanks, T. D. & Shadlen, M. N. Bounded integration in parietal cortex underlies decisions even when viewing duration is dictated by the environment. *J. Neurosci.* **28**, 3017–3029 (2008).

48. Kiani, R. & Shadlen, M. N. Representation of confidence associated with a decision by neurons in the parietal cortex. *Science* **324**, 759–764 (2009).

49. Inagaki, H. K. *et al.* Neural Algorithms and Circuits for Motor Planning. *Annu. Rev. Neurosci.* **45**, 249–271 (2022).

50. Meister, M. L. R., Hennig, J. A. & Huk, A. C. Signal multiplexing and single-neuron computations in lateral intraparietal area during decision-making. *J. Neurosci.* **33**, 2254–2267 (2013).

51. Park, I. M., Meister, M. L. R., Huk, A. C. & Pillow, J. W. Encoding and decoding in parietal cortex during

bioRxiv preprint doi: https://doi.org/10.1101/2023.10.15.562427; this version posted November 20, 2023. The copyright holder for this preprint (which was not certified by peer review) is the author/funder. All rights reserved. No reuse allowed without permission.

sensorimotor decision-making. *Nat. Neurosci.* **17**, 1395–1403 (2014).

52. Okazawa, G., Hatch, C. E., Mancoo, A., Machens, C. K. & Kiani, R. Representational geometry of perceptual decisions in the monkey parietal cortex. *Cell* **184**, 3748–3761.e18 (2021).
53. Charlton, J. A. & Goris, R. Abstract deliberation by visuomotor neurons in prefrontal cortex. *bioRxiv* 2022.12.06.519340 (2022) doi:10.1101/2022.12.06.519340.
54. Neri, P., Parker, A. J. & Blakemore, C. Probing the human stereoscopic system with reverse correlation. *Nature* **401**, 695–698 (1999).
55. Okazawa, G., Sha, L., Purcell, B. A. & Kiani, R. Psychophysical reverse correlation reflects both sensory and decision-making processes. *Nat. Commun.* **9**, 3479 (2018).
56. Odoemene, O., Pisupati, S., Nguyen, H. & Churchland, A. K. Visual Evidence Accumulation Guides Decision-Making in Unrestrained Mice. *J. Neurosci.* **38**, 10143–10155 (2018).
57. Brown, S. D. & Heathcote, A. The simplest complete model of choice response time: linear ballistic accumulation. *Cogn. Psychol.* **57**, 153–178 (2008).
58. Thura, D., Beauregard-Racine, J., Fradet, C.-W. & Cisek, P. Decision making by urgency gating: theory and experimental support. *J. Neurophysiol.* **108**, 2912–2930 (2012).
59. Yates, J. L., Park, I. M., Katz, L. N., Pillow, J. W. & Huk, A. C. Functional dissection of signal and noise in MT and LIP during decision-making. *Nat. Neurosci.* **20**, 1285–1292 (2017).
60. Scott, B. B. *et al.* Fronto-parietal Cortical Circuits Encode Accumulated Evidence with a Diversity of Timescales. *Neuron* **95**, 385–398.e5 (2017).
61. Shadlen, M. N. *et al.* Comment on 'Single-trial spike trains in parietal cortex reveal discrete steps during decision-making'. *Science* vol. 351 1406–1406 Preprint at https://doi.org/10.1126/science.aad3242 (2016).
62. Roitman, J. D. & Shadlen, M. N. Response of neurons in the lateral intraparietal area during a combined visual discrimination reaction time task. *J. Neurosci.* **22**, 9475–9489 (2002).
63. Stine, G. M., Trautmann, E. M., Jeurissen, D. & Shadlen, M. N. A neural mechanism for terminating decisions. *Neuron* (2023) doi:10.1016/j.neuron.2023.05.028.
64. Hernández-Navarro, L., Hermoso-Mendizabal, A., Duque, D., de la Rocha, J. & Hyafil, A. Proactive and reactive accumulation-to-bound processes compete during perceptual decisions. *Nat. Commun.* **12**, 7148

bioRxiv preprint doi: https://doi.org/10.1101/2023.10.15.562427; this version posted November 20, 2023. The copyright holder for this preprint (which was not certified by peer review) is the author/funder. All rights reserved. No reuse allowed without permission.

(2021).

65. Huk, A. C., Katz, L. N. & Yates, J. L. The Role of the Lateral Intraparietal Area in (the Study of) Decision Making. *Annu. Rev. Neurosci.* **40**, 349–372 (2017).
66. Joo, S. J., Katz, L. N. & Huk, A. C. Decision-related perturbations of decision-irrelevant eye movements. *Proc. Natl. Acad. Sci. U. S. A.* **113**, 1925–1930 (2016).
67. Harris, L. R. *et al.* How our body influences our perception of the world. *Front. Psychol.* **6**, 819 (2015).
68. Gold, J. I., Law, C.-T., Connolly, P. & Bennur, S. The relative influences of priors and sensory evidence on an oculomotor decision variable during perceptual learning. *J. Neurophysiol.* **100**, 2653–2668 (2008).
69. Urai, A. E., de Gee, J. W., Tsetsos, K. & Donner, T. H. Choice history biases subsequent evidence accumulation. *Elife* **8**, (2019).
70. Mendonça, A. G. *et al.* The impact of learning on perceptual decisions and its implication for speed-accuracy tradeoffs. *Nat. Commun.* **11**, 2757 (2020).

bioRxiv preprint doi: https://doi.org/10.1101/2023.10.15.562427; this version posted November 20, 2023. The copyright holder for this preprint (which was not certified by peer review) is the author/funder. All rights reserved. No reuse allowed without permission.

Methods

Contents

1 Subjects

The animal procedures described in this study were approved by the Princeton University Institutional Animal Care and Use Committee and were carried out in accordance with National Institutes of Health standards. All subjects were adult male Long-Evans rats (Taconic, NY) that were pair housed in Technoplast cages and were kept in a 12 hr reversed light-dark cycle. All training and testing procedures were conducted during the dark cycle. Rats had free access to food but had restricted water access. The amount of water that the rats obtained daily was at least 3% of their body weight.

bioRxiv preprint doi: https://doi.org/10.1101/2023.10.15.562427; this version posted November 20, 2023. The copyright holder for this preprint (which was not certified by peer review) is the author/funder. All rights reserved. No reuse allowed without permission.

2 Behavioral task

Rats performed the behavioral task in custom-made training enclosures (Island Motion, NY) placed inside sound- and light-attenuated chambers (IAC Acoustics, Naperville, IL). Each enclosure consisted of three straight walls and one curved wall in which three nose ports were embedded (one in the center and one on each side). Each nose port also contained one light-emitting diode (LED) that was used to deliver visual stimuli, and the front of the nose port was equipped with an infrared (IR) beam to detect the entrance of the rat's nose into the port. A loudspeaker was mounted above each of the side ports and was used to present auditory stimuli. Each of the side ports also contained a silicone tube that was used for water reward delivery, with the amount of water controlled by valve opening time.

Rats performed an auditory discrimination task in which optimal performance required the gradual accumulation of auditory clicks [1]. At the start of each trial, rats inserted their nose in the central port and maintained this placement for 1.5 s ("fixation period"). After a variable delay of 0.5-1.3 s, two trains of randomly timed auditory clicks were presented simultaneously, one from the left and one from the right speaker. At the beginning of each click train, a click was played simultaneously from the left and the right speaker a ("stereoclick") Regardless of onset time, the click trains terminated at the end of the fixation period, resulting in stimuli whose duration varied from 0.2-1 s. The train of clicks from each speaker was generated by an underlying Poisson process, with different mean rates for each side. The combined mean click rate was fixed at 40 Hz, and trial difficulty was manipulated by varying the ratio of the generative click rate between the two sides. The generative click rate ratio varied from 39:1 clicks/s (easiest) to 26:14 (most difficult). At the end of the fixation period, rats could orient towards the nose port on the side where more clicks were played and obtain a water reward.

Psychometric functions were computed by dividing trials into eight similarly sized groups according to the total difference in the right and left clicks, and for each group, computing the fraction of trials ending in a right choice. The confidence interval of the fraction of right response was computed using the Clopper-Pearson method.

3 Electrophysiological recording

Neurons were recorded using chronically implanted Neuropixels 1.0 probes that are recoverable after the experiment [4]. In each of four animals, a probe was implanted at 4.0 mm anterior to Bregma, 1.0 mm lateral, for a distance of 4.2 mm, and at an angle of 10 degrees relative to the sagittal plane intersecting the insertion site, such that the probe tip was more medial than the probe base. In each of five other animals, a probe was implanted to target primary motor cortex, dorsal striatum, and ventral striatum, at the site 1.0 mm anterior, 2.4 mm lateral, for a distance of 8.4 mm, and at an angle of 15 degrees relative to the coronal plane intersecting the insertion site, such that the probe tip was more anterior than the probe base. In each of three final set of rats, a probe was implanted to target the frontal orienting fields and anterior dorsal striatum at 1.9 mm anterior, 1.3 mm lateral, for a distance of 7.4 mm, and at angle of -10 degree relative to the sagittal plane intersecting the insertion site, such that the probe tip was more lateral than the probe base. Spikes were sorted into clusters using Kilosort2 [7], and clusters were manually curated. Different electrodes were recorded from across different days.

4 Muscimol inactivation

Infusion cannulas (Invivo1) were implanted bilaterally over dorsomedial frontal cortex (4.0 mm AP, 1.2 mm ML). After the animal recovered from surgery, the animal is anesthetized and on alternate days, a 600 nL solution of either only saline or muscimol (up to 150 nG) was infused in each hemisphere. Half an hour after the animal wakes up from anesthesia, the animal is allowed to perform the behavioral task.

5 Retrograde tracing

To characterize the anatomical inputs into dorsal striatum, 50 nL of cholera toxin subunit B conjugate (ThermoFisher Scientific) was injected into dorsal striatum at 1.9 mm AP, 2.4 ML, 3.5 mm below the cortical surface. The animal was perfused seven days after surgery.

bioRxiv preprint doi: https://doi.org/10.1101/2023.10.15.562427; this version posted November 20, 2023. The copyright holder for this preprint (which was not certified by peer review) is the author/funder. All rights reserved. No reuse allowed without permission.

6 Histology

The rat was fully anesthetized with 0.4 mL ketamine (100 mg/ml) and 0.2 mL xylazine (100 mg/ml) IP, followed by transcardial perfusion of 100 mL saline (0.9% NaCl, 0.3x PBS, pH 7.0, 0.05 mL heparin 10,000 USP units/mL), and finally transcardial perfusion of 250 mL 10% formalin neutral buffered solution (Sigma HT501128). The brain was removed and post fixed in 10% formalin solution for a minimum period of 7 days. 100 micrometer sections were prepared on a Leica VT1200S vibratome, and mounted on Superfrost Pus glass slides (Fisher) with Fluoromount-G (Southern Biotech) mounting solution and glass cover slips. Images were acquired on a Hamtasu NanoZoomer under 4x magnification.

7 Neuronal selection

Only neurons that meet a pre-selected threshold for being reliably choice selective are included for analysis. For each neuron, reliably in choice selectivity is measured using the area under the receiver operating characteristic (auROC) indexing how well an ideal observer can classify between a left- and right-choice trial based on the spike counts of the neuron. Spikes were counted in four non-overlapping time windows (0.01-0.21 s after stimulus onset, 0.21-0.4, 0.41-0.6, and 0.61-0.9), and an auROC was computed for each time window. A neuron with an auROC < 0.42 or > 0.58 for any of the these windows is deemed choice selective and included for analysis. Across sessions, the median fraction of neurons included under this criterion is 10.4%.

8 FINDR

Detailed description are provided in [3]. Briefly, to infer velocity vector fields (or flow fields) from the neural population spike trains, we used a sequential variational autoencoder (SVAE) called Flow-field inference from neural data using deep recurrent networks (FINDR).

At each time step ($\Delta t = 0.01s$), the firing rates of N simultaneously recorded neurons $\boldsymbol{r}_t$ are given by

$$\boldsymbol{r}_t = \text{softplus}(\boldsymbol{W}\boldsymbol{z}_t + \boldsymbol{b}_t) \tag{1}$$

where softplus is a function approximating the firing rate-synaptic current relationship (f-I curve) of neurons, $\boldsymbol{z}_t$ is a D-dimensional vector representing the latent decision variable, $\boldsymbol{W}$ a $N \times D$ matrix representing the encoding weights, $\boldsymbol{b}_t$ a N-dimensional vector representing the the decision-irrelevant baseline input. Conditioned on the value of the latent decision variable, the observed spike train response of each neuron at each time step is modeled as a Poisson random variable.

The discretized time derivative of the decision variable is given by

$$\frac{\boldsymbol{z}_{t+\Delta t} - \boldsymbol{z}_t}{\Delta t} = F(\boldsymbol{z}_t, \boldsymbol{u}_t) \tag{2}$$

where the input $\boldsymbol{u}_t$ is a two-dimensional vector representing the number of left and right clicks played on a time step. We obtain $\boldsymbol{z}_{t+\Delta t}$ from $\boldsymbol{z}_t$ and $\boldsymbol{u}_t$ using

$$\boldsymbol{z}_{t+\Delta t} = \boldsymbol{z}_t + \Delta t F(\boldsymbol{z}_t, \boldsymbol{u}_t) + \eta_t \tag{3}$$

where $\eta_t \sim \mathcal{N}(0, \Delta t \Sigma)$. Σ is a D-dimensional diagonal matrix. F is parametrized by a gated feedforward neural network, and Eq. (3) is an Euler-discretized gated neural stochastic differential equations (gnSDE) [2]. FINDR learns $\boldsymbol{W}$, $\boldsymbol{b}$, Σ, and the parameters of the neural network representing F, by maximizing the approximate lower bound of the log-likelihood of the simultaneously recorded spike trains, given the auditory clicks.

During optimization, FINDR learns an encoding function which transforms spiking neural data and experimental stimuli (which, in our case, are auditory clicks) into low-dimensional dynamical trajectories, and a decoding function that learns to reconstruct the spiking neural data from the low-dimensional trajectories. In addition, FINDR simultaneously infers the vector field in the latent state space that best describes the learned low-dimensional trajectories. During training, FINDR uses stochastic gradient descent (SGD) to minimize both the reconstruction of spiking neural data from low-dimensional dynamical trajectories, and the distance between the distribution of the inferred trajectories and the distribution of trajectories generated from the vector field. To arrive at our results, we optimized the hyperparameters of FINDR using hyperparameter grid-search, using the hyperparameter space described in [3]. The weight

bioRxiv preprint doi: https://doi.org/10.1101/2023.10.15.562427; this version posted November 20, 2023. The copyright holder for this preprint (which was not certified by peer review) is the author/funder. All rights reserved. No reuse allowed without permission.

on the vector-field inference objective c (in Equation (10) of [3]) is set to be 0.1 throughout the paper, except for fitting the dynamical system in Extended Data Fig. 3b, where $c = 0.0125$.

After optimization, because the same $\boldsymbol{r}_t$ can be given by different values of $\boldsymbol{W}$ and z_t, to uniquely identify the latent dynamics, we define

$$\tilde{z}_t = S\,V^\top z_t \tag{4}$$

where S is a $D \times D$ diagonal matrix containing the singular values of the inferred matrix W and V a $D \times D$ matrix containing the right singular vectors. To obtain meaningful axes for the transformed latent space, we generate 5000 different trajectories of $\tilde{z}$, and perform principal component analysis (PCA) on the trajectories. The principal components (PCs) were used to define the dimensions of the decision variable $\tilde{z}$. In all of our analyses, the latent trajectories and vector fields inferred by FINDR are in the transformed latent space.

9 Intrinsic and input dynamics

Our dynamical system can be written as

$$\dot{z} = F(z, \boldsymbol{u}), \tag{5}$$

where we separate the components of the dynamics $\dot{z}$ into the intrinsic, or input-independent, component:

$$\dot{z}_{\text{intrinsic}} = F(z, \boldsymbol{0}) \tag{6}$$

and the input-driven component:

$$\dot{z}_{\text{input}} = F(z, \boldsymbol{u}) - F(z, \boldsymbol{0}). \tag{7}$$

Note that $\dot{z} = \dot{z}_{\text{intrinsic}} + \dot{z}_{\text{input}}$. If the sensory stimulus $\boldsymbol{u}$ is presented continuously throughout the trial, Eq. (7) indeed describes the direction and magnitude of input (i.e., input vector) at a particular state z. For example, in a random dot motion (RDM) task [5], the coherence of the dots (or the evidence strength) may be represented as a 1-dimensional variable $\boldsymbol{u} \in [-1, 1]$, where -1 indicates 100% coherence leftward motion and 1 indicates 100% coherence rightward motion. However, if $\boldsymbol{u}$ is discrete and presented at random times in the trial, as in our task, $\boldsymbol{u}$ may be represented as a 2-dimensional variable where $\boldsymbol{u} = \boldsymbol{0} = [0; 0]$ when there is no click, $\boldsymbol{u} = [1; 0]$ when there is a left click, and $\boldsymbol{u} = [0; 1]$ when there is a right click. The crucial difference between an RDM task and our task is that in an RDM task, $\boldsymbol{u}$ typically stays fixed throughout the trial and encodes evidence strength, while in our task, $\boldsymbol{u}$ changes throughout the trial depending on whether there was a click or not, and does not itself encode evidence strength. What this means is that, for example, in our task, $\dot{z} = F(z, [1; 0]) - F(z, [0; 0])$ is similar to presenting a strong leftward evidence continuously throughout the trial (similar to giving a 100% coherence leftward motion in the RDM task). To correct for the fact that the value that $\boldsymbol{u}$ can take discretely and stochastically changes across time steps in a trial, and thus $p(\boldsymbol{u}|z)$ is different across the state space of z, we multiply $p(\boldsymbol{u}|z)$ to Eq. (7):

$$\dot{z}_{\text{input}} = p(\boldsymbol{u}|z)[F(z, \boldsymbol{u}) - F(z, \boldsymbol{0})]. \tag{8}$$

More specifically,

$$\begin{aligned} \dot{z}_{\text{left}} &= p(\boldsymbol{u} = [1; 0]|z)[F(z, \boldsymbol{u} = [1; 0]) - F(z, \boldsymbol{u} = [0; 0])], \\ \dot{z}_{\text{right}} &= p(\boldsymbol{u} = [0; 1]|z)[F(z, \boldsymbol{u} = [0; 1]) - F(z, \boldsymbol{u} = [0; 0])]. \end{aligned} \tag{9}$$

Note that we have separated the dynamics $\dot{z}$ into three distinct components – intrinsic dynamics, leftward input dynamics and rightward input dynamics. Adding Eq. (6) and Eq. (9), i.e., $\dot{z} = \dot{z}_{\text{intrinsic}} + \dot{z}_{\text{left}} + \dot{z}_{\text{right}}$, we have

$$\dot{z} = p(\boldsymbol{u} = [0; 0]|z)F(z, \boldsymbol{u} = [0; 0]) + p(\boldsymbol{u} = [1; 0]|z)F(z, \boldsymbol{u} = [1; 0]) + p(\boldsymbol{u} = [0; 1]|z)F(z, \boldsymbol{u} = [0; 1]). \tag{10}$$

Therefore, $\dot{z}$ gives us the overall dynamics $F(z, \boldsymbol{u})$ with an "effective" $\boldsymbol{u}$ that normalizes across the three possible values that $\boldsymbol{u}$ can take in a given z: $[0; 0]$, $[1; 0]$, $[0; 1]$.

To estimate $p(\boldsymbol{u}|z)$, we generate click trains for 5000 trials in a way that is similar to how clicks are generated for the task done by our rats. Then, we simulate 5000 latent trajectories from F and the generated click trains. We then bin the state space of z and ask, for a single bin, how many times the latent trajectories cross that bin in total and how many of the latent trajectories, when crossing that bin had $\boldsymbol{u} = [1; 0]$ or $\boldsymbol{u} = [0; 1]$. That is, we estimate $p(\boldsymbol{u} = [1; 0]|z)$ with $\frac{\#\text{ of latent states with } \boldsymbol{u}=[1;0] \text{ in the bin that covers } z}{\#\text{ of latent states in the bin that covers } z}$. For Fig. 2 in the main text, because z is 2-dimensional, we use bins of 8-by-8

bioRxiv preprint doi: https://doi.org/10.1101/2023.10.15.562427; this version posted November 20, 2023. The copyright holder for this preprint (which was not certified by peer review) is the author/funder. All rights reserved. No reuse allowed without permission.

that cover the state space traversed by the 5000 latent trajectories, and weigh the flow arrows of the input dynamics with the estimated $p(\boldsymbol{u}|z)$. Similarly, for the background shading that quantifies the speed of input dynamics in Fig. 2, we use bins of 100-by-100 to estimate $p(\boldsymbol{u}|z)$, and apply a Gaussian filter with $\sigma = 2$ to smooth the histogram. A similar procedure was done in Extended Data Fig. 3 and 6 to estimate $p(\boldsymbol{u}|z)$.

10 Multi-mode drift-diffusion model (MMDDM)

A detailed account is provided in the Supplementary Information. Briefly, the MMDDM is an autoregressive, input-output hidden-Markov model (HMM) whose emissions consists of the spike train responses of simultaneously recorded neurons and the behavioral choice. The latent variable has transition dynamics that are modelled as a Orstein-Uhlenbeck process [1] to express drift-diffusion dynamics. The transition matrix at each time step is computed by using the Fokker-Planck equations to obtain the conditional forward propagation distributions and then discretizing the forward distributions. The transition matrix (as well as the prior probability vector of the latent variable) is specified by only three free parameters–bound height, initial value, and the signal-to-noise ratio of the input–that are learned separately for each recording session.

The emissions of the MMDDM are the spike train responses at each time step of the all simultaneously recorded neurons and the behavioral choice. On each time step, given the value of the latent variable, the conditional spike train response is modelled as Poisson generalized linear models (GLM). The GLM allows us to mitigate potential omitted variable bias by incorporating nuisance variables as input to the neural spike trains. These nuisance variables include the spike history and choice-independent baseline changes aligned to stimulus onset and movement onset. Slow fluctuations in baseline across trials are also incorporated. The spike train response at each time step depends on the latent variable on only that time step and no other time step.

Each neuron relates to the latent variable through two scalar weights, w_{EA} and w_{DC} , that specifies the encoding of the latent variable during the evidence integration phase and the choice maintenance phase, respectively. When the latent variable has not yet reached the bound, all simultaneously recorded neurons encode the latent variable through their own w_{EA}, and when the bound is reached, their own w_{DC}. Separate w_{EA} and w_{DC} are learned for each neuron.

The behavioral choice is specified by the sign of on the value of the latent variable on the last time step of the trial (positive = rightward).

All parameters, including the three parameters of the latent variable, as well as the eleven parameters private to each neuron, are learned simultaneously by jointly fitting to all spike trains and choices. To fit the model, the analytic gradient of the log-likelihood is computed using the forward-backward algorithm. Models were fit using five-fold cross-validation.

The engagement index (EI) was computed for each neuron on the basis of its w_{EA} and w_{DC}: $EI \equiv (|w_{EA}| - |w_{DC}|)/(|w_{EA}| + |w_{DC}|)$. The index is based on the widely used modulation index used in analyses in systems neuroscience. It ranges from -1 to 1. A neuron with an EI near -1 encodes the latent variable only during choice maintenance; a neuron with an EI near 0 encodes the latent variable similarly during evidence accumulation and choice maintenance; and an EI near 1 indicates encoding only during evidence accumulation.

11 Peri-stimulus time histogram (PSTH)

Spike times were binned at 0.01 s and included spikes up to one second after the onset of the auditory stimulus (click trains) until one second after the stimulus onset, or until when the animal removed its nose the central port, whichever came first. The time-varying firing rate of of each neuron in each group of trials (i.e., task condition) was estimated with a peristimulus time histogram (PSTH), which was computed by convolving the spike train on each trial with a causal gaussian linear filter with a standard deviation of 0.1 s and a width of 0.3 s and averaging across trials. The confidence interval of a PSTH was computed by bootstrapping across trials. The normalized PSTH of each neuron in each task condition was computed by dividing the PSTH by the mean firing rate of that neuron across all time steps across all trials. Trials were grouped by the animal's choice and/or the generative click rate ratio. A "preferred" task condition was defined for each neuron as the group of trials with the behavioral choice when the neuron responded more strongly, and a "null" task condition was defined as the trials associated with the other choice. The aggregate PSTHs across neurons was computed by averaging across the PSTH for either the preferred or null task condition.

bioRxiv preprint doi: https://doi.org/10.1101/2023.10.15.562427; this version posted November 20, 2023. The copyright holder for this preprint (which was not certified by peer review) is the author/funder. All rights reserved. No reuse allowed without permission.

12 Choice selectivity

In figure 5b and Extended data figure 8i, for each neuron, and for each each time step t aligned to the onset of the auditory click trains, we computed choice selectivity $c(t)$:

$$c(t) \equiv \frac{r(t) - l(t)}{r(t^*) - l(t^*)} \tag{11}$$

where r and l are the PSTH's computed from trials ending in a right and left choice, respectively. The time step t^* is time of the maximum absolute difference:

$$t^* \equiv \underset{t}{\operatorname{argmax}} |r(t) - l(t)| \tag{12}$$

In Extended data figure 8i, neurons are sorted by the center of mass of each neuron's absolute value of the choice selectivity.

13 Trial-averaged trajectories in neural state space

To measure the trial-averaged dynamics in neural state space, principal component analysis (PCA) was performed on a data matrix made by concatenating the peri-stimulus time histograms. The data matrix X has dimensions $T \times C$-by-N, where T is the number of time steps ($T = 100$), C is the number of task conditions ($C = 2$ for choice-conditioned PSTHs, $C = 4$ for PSTHs conditioned on both choice and evidence strength), and N is the number of neurons. The mean across rows is subtracted from X, and singular value decomposition is performed: $USV^\top = X$. The principal axes correspond to the columns of the right singular matrix V, and the projections of the original data matrix X onto the principal axes correspond to the left singular matrix (U) multiplied by S, the rectangular diagonal matrix of singular values. The first two columns of the projections US are plotted as the trajectories in neural state space.

14 MMDDM-inferred time of decision commitment

The time step when decision commitment occurred is selected to be when the posterior probability of the latent variable at either the left or the right bound, given the learned MMDDM parameters, click times, spike trains, and behavioral choice, to be greater than 0.8. Results were similar for other thresholds, and the particular threshold of 0.8 was chosen to balance between the accuracy of the prediction and the number of trials for which commitment is predicted to have occurred. Under definition, commitment occurred on 34.6% of the trials. The MMDDM parameters were learned using training data in five-fold cross-validation.

15 Peri-commitment time histograms (PCTH)

On trials for which a time of decision commitment could be detected (see section 14), the spike train are aligned to the predicted time of commitment and then averaged across those trials. The trial-average is then filtered with a causal Gaussian kernel with a standard deviation of 0.05s. The PCTH were averaged within each of three groups of neurons: 1) neurons that are similar engaged in evidence accumulation and choice maintenance; 2) neurons more strongly engaged in evidence accumulation; and 3) neurons more strongly engaged in choice maintenance. Each neuron was assigned to one of these groups according to its engagement index (EI; see section 10). Neurons with $-\frac{1}{3} \leq EI < \frac{1}{3}$ are considered to be similarly engaged in evidence accumulation and choice maintenance; neurons with $EI \geq \frac{1}{3}$ are considered to be more strongly engaged in evidence accumulation; and those with $EI < -\frac{1}{3}$ are considered to be more strongly engaged in choice maintenance. Principal component analysis on the PCTH's are performed as described in section 13.

For this analysis, we focused on only the 65/115 sessions for which the MMDDM improves the R^2 of the PSTH's and also that the inferred encoding weights are reliable across cross-validation folds ($R^2 > 0.9$). From this subset of sessions, there were 1,116 neurons similarly engaged in maintenance and accumulation, 414 neurons that are more engaged in maintenance, and 1,529 neurons more engaged in accumulation.

To compute the shuffled PCTH, the predicted times of commitment are shuffled among only the trials on which commitment were detected. If the randomly assigned commitment time extends beyond the length of the trial, then the time of commitment is assigned to be the last time step of that trial.

bioRxiv preprint doi: https://doi.org/10.1101/2023.10.15.562427; this version posted November 20, 2023. The copyright holder for this preprint (which was not certified by peer review) is the author/funder. All rights reserved. No reuse allowed without permission.

16 Psychophysical kernel

We extended the logistic model [6] for inferring the psychophysical kernel to include a lapse parameter and also temporal basis functions to parametrize the kernel. Cross-validated model comparison was performed to select the optimal type and number of temporal basis functions. A detailed account of the model is provided in the Supplemental Information.

17 Statistical tests

Binomial confidence intervals were computed using the Clopper-Pearson method. All other confidence intervals were computed through a bootstrapping procedure using the bias corrected and accelerated percentile method [8]. *P*-values comparing medians were computed using a two-sided Wilcoxon rank sum test, which tests the null hypothesis that two independent samples are from continuous distributions with equal medians, against the alternative that they are not.

References

[1] B. W. Brunton, M. M. Botvinick, and C. D. Brody. Rats and humans can optimally accumulate evidence for decision-making. *Science*, 340(6128):95–98, 2013.

[2] Timothy Doyeon Kim, Tankut Can, and Kamesh Krishnamurthy. Trainability, Expressivity and Interpretability in Gated Neural ODEs. *Proceedings of the 40th International Conference on Machine Learning*, 2023.

[3] Timothy Doyeon Kim, Thomas Zhihao Luo, Tankut Can, Kamesh Krishnamurthy, Jonathan W. Pillow, and Carlos D. Brody. Flow-field inference from neural data using deep recurrent networks. *bioRxiv*, 2023.

[4] Thomas Zhihao Luo, Adrian Gopnik Bondy, Diksha Gupta, Verity Alexander Elliott, Charles D. Kopec, and Carlos D. Brody. An approach for long-term, multi-probe neuropixels recordings in unrestrained rats. *Elife*, 2020.

[5] William T. Newsome, Kenneth H. Britten, and J. Anthony Movshon. Neuronal correlates of a perceptual decision. *Nature*, 341, 1989.

[6] O. Odoemene, S. Pisupati, H. Nguyen, and A. K. Churchland. Visual evidence accumulation guides decision-making in unrestrained mice. *Journal of Neuroscience*, 2018.

[7] M. Pachitariu, N. A. Steinmetz, S. N. Kadir, M. Carandini, and K. D Harris. Fast and accurate spike sorting of high-channel count probes with kilosort. *Advances in neural information processing systems*, 29, 2016.

[8] Ryan J. Tibshirani and Bradley Efron. *An Introduction to the Bootstrap*. Chapman Hall/CRC, 1994.

bioRxiv preprint doi: https://doi.org/10.1101/2023.10.15.562427; this version posted November 20, 2023. The copyright holder for this preprint (which was not certified by peer review) is the author/funder. All rights reserved. No reuse allowed without permission.

Supplementary information

Contents

1 Simulations of the canonical and non-canonical attractor hypotheses

The dynamical equations for each of the attractor hypotheses used to generate the flow fields in Fig. 1 and Extended Data Fig. 1, and synthetic datasets in Extended Data Fig. 3 are as follows.

Bistable attractors:

$$\begin{aligned} dz_1 &= 10z_1(0.7 + z_1)(0.7 - z_1)dt + cudt + dW \\ dz_2 &= -10z_2dt + dW \end{aligned} \tag{1}$$

Classic DDM:

$$\begin{aligned} dz_1 &= \begin{cases} cudt + 0.5dW, & z_1 \in (-0.7, 0.7) \\ 10z_1(0.7 - z_1)(0.7 + z_1)dt + 0.5dW, & z_1 \notin (-0.7, 0.7) \end{cases} \\ dz_2 &= -30z_2 + 0.5dW \end{aligned} \tag{2}$$

bioRxiv preprint doi: https://doi.org/10.1101/2023.10.15.562427; this version posted November 20, 2023. The copyright holder for this preprint (which was not certified by peer review) is the author/funder. All rights reserved. No reuse allowed without permission.

RNN line attractor:

$$\begin{aligned} dz_1 &= 5z_2 + dW \\ dz_2 &= -5z_2 dt + cudt + dW \end{aligned} \tag{3}$$

Non-canonical:

$$\begin{aligned} dz_1 &= 5z_1(0.85 + z_1)(0.85 - z_1)dt + cudt + dW \\ dz_2 &= 5(0.5|z_1| + 0.1)(z_1 - 1.2z_2) + dW \end{aligned} \tag{4}$$

Here, u at each time point can take a value from the set $\{-1, 0, 1\}$, where -1 indicates a leftward click, 0 indicates no click, and 1 indicates a rightward click. $c = 1/10$ for RNN line attractor, and $c = 1/40$ for others. Similar to the task done by our rats, for each trial, γ was drawn from the set $\{-3.5, -2.5, -1.5, -0.5, 0.5, 1.5, 2.5, 3.5\}$. We generated left and right clicks with rates $40/(1 + \exp(\gamma))$ and $40/(1 + \exp(-\gamma))$, respectively. The total duration of each trial was $1s$, and the duration of the click stimulus was randomly chosen to be one of $0.5s$, $0.7s$, and $0.9s$ for each trial. We generated 500 trajectories from each of Eq. (1–4), and assumed that the initial condition $\boldsymbol{z}(0) = \mathbf{0}$. Each trajectory corresponds to a trial. The spikes were generated from

$$\begin{aligned} W_{ij} &\sim 1 + 5\mathcal{N}(0, 1) \\ r_i &= \text{softplus}\left(\sum_j W_{ij} z_j + 5\right) \\ x_i &\sim \text{Poisson}(\Delta t \cdot r_i) \end{aligned} \tag{5}$$

where $\boldsymbol{W} \in \mathbb{R}^{80\times 2}$, and x_i is the number of spikes in a time bin with width $\Delta t = 0.01s$. Therefore, a total of 80 neurons and 500 trials were simulated for each dataset.

2 Multi-mode drift-diffusion model (MMDDM)

2.1 Latent decision variable

The multi-mode drift-dffusion model (MMDDM) assumes that the decision-related component of the neural responses across multiple brain regions, as well as the animal's behavioral choice, are determined by a one-dimensional latent decision variable z. Following previous work [3, 4], we formulate the dynamics of z as an Ornstein-Uhlenbeck process, whose time evolution can be represented using the Fokker-Planck equation

$$dz = \begin{cases} 0, & z \in \{-B, B\} \\ (\lambda z + u)dt + \sigma_z dW, & z \in (-B, B) \end{cases} \tag{6}$$

When z is at either the left bound $-B$ or the right B, its value does not change. The bound height parameter $B \in (10, 20)$ is learned from the data.

The hyperparameter λ quantifies the consistent drift in z. For $\lambda < 0$, the integration is leaky, z drifts toward 0, and early inputs affect z less than later inputs. For $\lambda > 0$, z positively feedbacks to itself, z is impulsive, and early inputs affect z more than later inputs. The time constant of z is $1/\lambda$. In the case of $\lambda = 0$, z behaves in the regime of the drift-diffusion model. To implement either the MMDDM or the classic neural DDM, we set λ to be 0.

The momentary input u is given by by the difference between the input from the right and left clicks:

$$u(t) = c_R(t) - c_L(t) \tag{7}$$

The input from each click is given by

$$c(t) = \sum_{\tau\in\boldsymbol{\tau}} \delta(\tau - t) \cdot \zeta \cdot C(t) \tag{8}$$

where $\delta(x)$ is the Direct delta function, which has a value of 0 everywhere except for $\delta(x = 0)$, which occurs when x is equal to one of the elements in the set $\boldsymbol{\tau}$ containing the times of either the left or right clicks. For $\tau \in \boldsymbol{\tau}$

$$\int_{t-dt/2}^{t+dt/2} \delta(\tau - t)dx = 1 \tag{9}$$

bioRxiv preprint doi: https://doi.org/10.1101/2023.10.15.562427; this version posted November 20, 2023. The copyright holder for this preprint (which was not certified by peer review) is the author/funder. All rights reserved. No reuse allowed without permission.

The momentary input is corrupted by multiplicative noise ξ, a sample from the Gaussian distribution:

$$\zeta \sim \mathcal{N}(1, \sigma_s^2) \tag{10}$$

The free parameter $\sigma_s^2 \in (0.1, 20)$ quantifies the noise-to-signal ratio of the sensory input and is optimized during model fitting. To account for sensory adaptation, the momentary input is depressed by preceding clicks, and its magnitude is multiplicatively scaled by $C(t)$ (see section 2.1.4).

In the absence of feedback ($\lambda = 0$) and no momentary input, the variable z evolves stochastically due to the diffusion noise $\sigma_z dW$, where dW is a white noise Weiner process. Following previous findings [3], diffusion noise is fixed to be small by setting $\sigma_z = 1$ to be a hyperparameter.

2.1.1 Transition probability

The solution to the Fokker-Planck equations in Eq. 6 provides the transition probability of z:

$$p(z_t \mid z_{t-1}) = \begin{cases} 1, & z_{t-1} = z_t = -B \\ 1, & z_{t-1} = z_t = B \\ f(z_t \mid \mu_t, \sigma_t^2), & (z_{t-1}, z_t) \in (-B, B) \\ \int_{-\infty}^{-B} f(x \mid \mu_t, \sigma_t^2)\, dx, & z_t = -B, z_{t-1} \in (-B, B) \\ \int_{B}^{\infty} f(x \mid \mu_t, \sigma_t^2)\, dx, & z_t = B, z_{t-1} \in (-B, B) \\ 0, & \text{otherwise} \end{cases} \tag{11}$$

If z is at either of the two absorbing bounds (i.e, $-B$ or B) in the previous time step, then z must retain the same value for the current time step. If both the previous and present values are within the bounds, the probability is given by a Gaussian distribution with mean μ_t and variance σ_t^2:

$$f(x \mid \mu_t, \sigma_t^2) \sim \mathcal{N}(\mu_t, \sigma_t^2) \tag{12}$$

$$\mu_t = e^{\lambda dt}\left(z_{t-1} + \frac{v_t}{\lambda dt}\right) - \frac{v_t}{\lambda dt} \tag{13}$$

where v is expectation of the difference between the sum of the right and left click inputs:

$$v = \sum_{\tau_R \in [t-dt, t)} C(\tau_R) - \sum_{\tau_L \in [t-dt, t)} C(\tau_L) \tag{14}$$

In the limit of λ toward 0, the mean μ_t is given by

$$\lim_{\lambda \to 0} \mu_t = z_{t-1} e^{\lambda dt} + v_t\left(1 - e^{-\lambda dt}\right) \tag{15}$$

The variance σ_t^2 is a sum of the stimulus-independent diffusion noise and the noise emanating from each click

$$\sigma_t^2 = \sigma_z^2 dt + \sigma_s^2 \left[\sum_{\tau_R \in [t-dt, t)} C(\tau_R) + \sum_{\tau_L \in [t-dt, t)} C(\tau_L) \right] \tag{16}$$

2.1.2 Prior probability

The prior probability is given by

$$p(z_1) = \begin{cases} f(z_1 \mid \mu_1, \sigma_1^2), & B > z_1 > -B \\ \int_{-\infty}^{-B} f(x \mid \mu_1, \sigma_1^2)\, dx, & z_1 = -B \\ \int_{B}^{\infty} f(x \mid \mu_1, \sigma_1^2)\, dx, & z_1 = B \end{cases} \tag{17}$$

Where

$$f(x \mid \mu_1, \sigma_1^2) \sim \mathcal{N}(\mu_1, \sigma_1^2) \tag{18}$$

The mean of the Gaussian distribution is specified by the parameter $\mu_1 \in (-5, 5)$, which is learned from the data, and the variance is a hyperparameter fixed to $\sigma_1^2 = 1$.

bioRxiv preprint doi: https://doi.org/10.1101/2023.10.15.562427; this version posted November 20, 2023. The copyright holder for this preprint (which was not certified by peer review) is the author/funder. All rights reserved. No reuse allowed without permission.

2.1.3 Discretization of time and decision variable

Similar to previous studies[3, 4], the model is implemented by discretizing both time and the decision variable z. Time is discretized to $\Delta t = 0.01$s, and the value of z is discretized to $\Xi = 53$ values equally spaced in $[-B, B]$. The i-th bin ξ_i is given by

$$\xi_i = \frac{2i - \Xi - 1}{\Xi - 1} B \tag{19}$$

The difference between successive bins is

$$\Delta\xi = \frac{2B}{\Xi - 1} \tag{20}$$

Under this discretization scheme, the probability $p(z)$ at each time step is represented by a Ξ-element probability vector $\boldsymbol{p}$ whose first element indicates the probability of z at the left bound, the last element the probability at the right bound, and the intervening elements correspond to the approximate probability at each bin. By definition of being of a probability vector, the elements of $\boldsymbol{p}$ always sum to 1. For each value z, the probability $p(z)$ is divided between the two closest bins, weighted by the relative distance between z and the two bins.

Prior probability vector To illustrate the discretization in detail, below we demonstrate the computation of the prior probability vector. Each element of the probability vector is computed as a definite integral of the normal distribution in Eq. (17). For the first element of the prior probability vector, which quantifies the probability of z at the left bound:

$$\boldsymbol{p}_{i=1} = \int_{-\infty}^{\xi_1} f(x; \mu_1, \sigma_1^2)\, dx + \frac{1}{\Delta\xi}\left[\int_{\xi_1}^{\xi_2} f(x; \mu_1, \sigma_1^2)\,(\xi_2 - x)\, dx\right] \tag{21}$$

The definite integral is equal to

$$\boldsymbol{p}_{i=1} = \Phi(\bar{z}_1) + \frac{\sigma_1}{\Delta\xi}\left\{\bar{z}_2\left[\Phi(\bar{z}_2) - \Phi(\bar{z}_1)\right] + \phi(\bar{z}_2) - \phi(\bar{z}_1)\right\} \tag{22}$$

where $\bar{z}_i$ is the z-score

$$\bar{z}_i = \frac{\xi_i - \mu_1}{\sigma_1}$$

and $\Phi(x)$ and ϕ are the standard normal cumulative distribution function and standard normal probability density function, respectively. The mean μ_1 and the standard deviation σ_1 are parameters of the model. For the second to second-to-last elements of the probability vector, i.e., $i \in \{2, ...\Xi - 1\}$:

$$\boldsymbol{p}_i = \frac{\sigma_1}{\Delta\xi}\left\{\bar{z}_{i+1}\left[\Phi(\bar{z}_{i+1}) - \Phi(\bar{z}_i)\right] + \bar{z}_{i-1}\left[\Phi(\bar{z}_{i-1}) - \Phi(\bar{z}_i)\right] + \phi(\bar{z}_{i+1}) + \phi(\bar{z}_{i-1}) - 2\phi(\bar{z}_i)\right\} \tag{23}$$

Finally, for the last element:

$$\boldsymbol{p}_\Xi = 1 - \Phi(\bar{z}_\Xi) + \frac{\sigma_1}{\Delta\xi}\left\{\bar{z}_{\Xi-1}\left[\Phi(\xi_{\Xi-1}) - \Phi(\xi_\Xi)\right] + \phi(\bar{z}_{\Xi-1}) - \phi(\bar{z}_\Xi)\right\} \tag{24}$$

Stochastic matrix The transition probability of z in Eq. (11) is represented as a square $\Xi \times \Xi$ stochastic matrix:

$$Z_t \approx p(z_t \mid z_{t-1}) \tag{25}$$

Each column of the matrix corresponds to the a probability vector corresponding to the conditional probability given the value of z on the preceding time step:

$$Z_t[:, j] \approx p(z_t \mid z_{t-1} = \xi_j) \tag{26}$$

Each element of the transition matrix is the conditional probability

$$Z_t[i, j] \approx p(z_t = \xi_i \mid z_{t-1} = \xi_j) \tag{27}$$

bioRxiv preprint doi: https://doi.org/10.1101/2023.10.15.562427; this version posted November 20, 2023. The copyright holder for this preprint (which was not certified by peer review) is the author/funder. All rights reserved. No reuse allowed without permission.

The first column of the transition matrix represents the conditional transition probability given that z was at the bound on the previous time step. By the definition of the absorbing bounds, for all time step t, the first column of the transition matrix has a value at the first row element and zero elsewhere.

$$Z[i,1] = \begin{cases} 1, & i = 1 \\ 0, & \text{otherwise} \end{cases} \tag{28}$$

Similarly, the last column of has a value of 1 at the last element and zero elsewhere:

$$Z[i,\Xi] = \begin{cases} 1, & i = \Xi \\ 0, & \text{otherwise} \end{cases} \tag{29}$$

Each of the intervening columns is computed similarly to the prior probability vector, but with a different Gaussian mean μ_j and variance σ^2. For $j \in \{2, ...\Xi - 1\}$. Both μ_j and σ^2 vary across time steps, but the subscript t is omitted for clarity.

$$Z_t[i,j] = \begin{cases} \Phi(\bar{z}_1) + \frac{\sigma_t}{\Delta\xi}\Big(\bar{z}_2\left[\Phi(\bar{z}_2) - \Phi(\bar{z}_1)\right] + \phi(\bar{z}_2) - \phi(\bar{z}_1)\Big), & i = 1 \\ \frac{\sigma_t}{\Delta\xi}\Big(\bar{z}_{i+1}\left[\Phi(\bar{z}_{i+1}) - \Phi(z_i)\right] + z_{i-1}\left[\Phi(\bar{z}_{i-1}) - \Phi(\bar{z}_i)\right] + \phi(\bar{z}_{i+1}) + \phi(\bar{z}_{i-1}) - 2\phi(\bar{z}_i)\Big), & \Xi > i > 1 \\ 1 - \Phi(\bar{z}_\Xi) + \frac{\sigma_t}{\Delta\xi}\Big(z_{\Xi-1}\left[\Phi(\xi_{\Xi-1}) - \Phi(\xi_\Xi)\right] + \phi(\bar{z}_{\Xi-1}) - \phi(\bar{z}_\Xi)\Big), & i = \Xi \end{cases} \tag{30}$$

where

$$\bar{z}_i = \frac{\xi_i - \mu_j}{\sigma}$$

The mean of the Gaussian is given by

$$\mu_j = e^{\lambda\Delta t}\left(\xi_j + \frac{v}{\lambda\Delta t}\right) - \frac{v}{\lambda\Delta t} \tag{31}$$

where v is expectation of the difference between the sum of the right and left click inputs:

$$v = \sum_{\tau_R \in [t-\Delta t, t)} C(\tau_R) - \sum_{\tau_L \in [t-\Delta t, t)} C(\tau_L) \tag{32}$$

Where τ_R are the times when a right click occurred, and τ_L where a left click occurred, and the $C(t)$ the post-adaptation strength of each click (see section 2.1.4).

The variance σ^2 does not vary across the columns of the transition matrix and a sum of the stimulus-independent diffusion noise and the noise emanating from each click

$$\sigma^2 = \sigma_z^2 \Delta t + \sigma_s^2 \left[\sum_{\tau_R \in [t-\Delta t, t)} C(\tau_R) + \sum_{\tau_L \in [t-\Delta t, t)} C(\tau_L) \right] \tag{33}$$

Because the momentary click input varies across time step, and because both μ_j and σ^2 depend on the momentary input.

2.1.4 Sensory adaptation

Sensory adaptation is conceptualized as nearly full depression immediately after a click and gradually less and less depression after the preceding click. This idea is modelled with the ordinary differential equation parametrizing the gain C of the momentary input

$$\frac{dC}{dt} = C \cdot (\phi - 1) \cdot \delta(\boldsymbol{\tau}_{L,R} - t) + k(1 - C) \tag{34}$$

with initial condition

$$C(t = 0) = 1 \tag{35}$$

bioRxiv preprint doi: https://doi.org/10.1101/2023.10.15.562427; this version posted November 20, 2023. The copyright holder for this preprint (which was not certified by peer review) is the author/funder. All rights reserved. No reuse allowed without permission.

At the occurrence of the first click on each trial, which is always the stereoclick, the gain of the momentary input is given by

$$C(dt) = \phi$$

In accordance with previous findings [3] and the behavioral and neural phenomena associated with the precedence effect[2], the hyperparameter ϕ is fixed to be 0.001. After the occurrence of a click, in the gap of time before the subsequent click, the gain recovers toward 1 with the exponential change rate k. We specify the change to be fast by setting $k = 100$.

After each click at time τ, the dynamics of C at time $\tau+\Delta t$ before any other click's arrival is computed by separately integrating over the intervals $[\tau, \tau + \epsilon]$ and $(\tau + \epsilon, \tau + \Delta t]$ for small $\epsilon \ll \Delta t$:

$$\int_{\tau}^{\tau+\epsilon} dC = k\int_{\tau}^{\tau+\epsilon} [1 - C(t)]dt + \int_{\tau}^{\tau+\epsilon} (\phi - 1)\delta(\tau - t)C(t)dt$$
$$C(\tau + \epsilon) - C(\tau) \approx k[1 - C(\tau + \epsilon) - 1 + C(\tau)]\epsilon + (\phi - 1)C(\tau)$$
$$C(\tau + \epsilon) \approx C(\tau) + k\epsilon[C(\tau) - C(\tau + \epsilon)] + (\phi - 1)C(0)$$
$$C(\tau + \epsilon) \approx C(\tau)\left[\phi + k\epsilon\left(1 - \frac{C(\tau + \epsilon)}{C(\tau)}\right)\right]$$

Integrating over the second interval,

$$\int_{\tau+\epsilon}^{\tau+\Delta t} \frac{dC}{1 - C(t)} = \int_{\tau+\epsilon}^{\tau+\Delta t} kdt + \int_{\tau+\epsilon}^{\tau+\Delta t} (\phi - 1)\delta(\tau - t)\frac{C(t)}{1 - C(t)}dt$$
$$- \log(|1 - C(\tau + \Delta t)|) + \log(|1 - C(\tau + \epsilon)|) = k(\Delta t - \epsilon)$$

Using the result obtained by integrating over the first interval,

$$|1 - C(\tau + \Delta t)| = \exp\left(\log(|1 - C(\tau + \epsilon)|) - k(\Delta t - \epsilon)\right)$$
$$|1 - C(\tau + \Delta t)| = |1 - C(\tau + \epsilon)| \exp\left(-k(\Delta t - \epsilon)\right)$$
$$|1 - C(\tau + \Delta t)| \approx \left|1 - C(\tau)\left[\phi + k\epsilon\left(1 - \frac{C(\tau + \epsilon)}{C(\tau)}\right)\right]\right| \exp\left(-k(\Delta t - \epsilon)\right)$$

In the limit of $\epsilon \to 0$,

$$|1 - C(\tau + \Delta t)| = |1 - \phi C(\tau + \Delta t)| \exp\left(-k\Delta t\right)$$

Therefore,

$$C(\tau + \Delta t) = \begin{cases} 1 - [1 - \phi C(\tau)] \exp\left(-k\Delta t\right) \\ 1 + [1 - \phi C(\tau)] \exp\left(-k\Delta t\right) \end{cases}$$

These two possibilities are disambiguated by the requirements

$$k \geq 0$$
$$\phi \in [0, 1]$$
$$C \in [0, 1]$$
$$C(0) = 1$$

Therefore

$$C(\tau + \Delta t) = 1 - [1 - \phi C(\tau)] \exp\left(-k\Delta t\right) \tag{36}$$

Note that if we take the derivative, we recover

$$\frac{dC}{dt} = k(1 - C)$$

For click times τ, the dynamics of C at the moment of each click can be computed recursively:

$$C(\tau_1) \equiv 1$$
$$C(\tau_2) = 1 - [1 - \phi] \exp\left[-k(\tau_2 - \tau_1)\right]$$
$$C(\tau_3) = 1 - [1 - \phi C(\tau_2)] \exp\left[-k(\tau_3 - \tau_2)\right]$$
$$\ldots$$

bioRxiv preprint doi: https://doi.org/10.1101/2023.10.15.562427; this version posted November 20, 2023. The copyright holder for this preprint (which was not certified by peer review) is the author/funder. All rights reserved. No reuse allowed without permission.

2.1.5 Latency

The clicks have a latency of Δt=0.01 s, set based on the latency of auditory responses in rat primary auditory cortex [14]. On time step t, the latent decision variable z receives input from clicks that occurred during $[t - 2\Delta t, t - \Delta t)$. Results are not affected by the exact value of the latency.

2.2 Spike train response

Conditioned on the decision variable z, each neuron's spike train response y is modelled as Poisson random variable:

$$p(y \mid z) = (\lambda \Delta t)^y \exp(-\lambda \Delta t)/y! \tag{37}$$

The spike train is binned at the time steps of $\Delta t = 0.01$ s, the same as that of the latent variable z. The firing rate λ is the nonlinearly rectified output of the softplus function (h), which approximates the neuronal frequency-current curve of a neuron:

$$h(x) = \log\{1 + \exp(x)\} \tag{38}$$

When the input x is very negative, $h(x)$ is approximately zero. When x is large and positive, $h(x)$ is approximately x itself. The same activation function is used for all neurons.

2.2.1 Decision-dependent predictor

The input x varies on each time step t on each trial and is a linear combination of the latent variable $z(t)$ and decision-independent baseline input $b(t)$

$$x(t) = w_z \cdot \tilde{z}(t) + b(t) \tag{39}$$

To maximize interpretability and minimize trade-offs between parameters, the value of z being encoded is independent of the bound height:

$$\tilde{z}_i \equiv \frac{z_i}{B} = \frac{2i - \Xi - 1}{\Xi - 1} \tag{40}$$

The weight of z depends on the state i of z itself:

$$w_z = \begin{cases} w_{DC} & \text{if } z \text{ is at a bound, i.e., } i = 1 \text{ or } i = \Xi \\ w_{EA} & \text{otherwise} \end{cases} \tag{41}$$

Each neuron has its own scalar w_{DC} and w_{EA}. Importantly, the neurons do not receive any direct input from the auditory clicks. The decision-independent baseline input $b(t)$ is a weighted sum of decision-independent predictors.

2.2.2 Decision-independent, within-trial varying predictors

The decision-independent predictors consist of four types of variables, three of which vary both within and across trials, and a fourth that varies only across trials.

Each within-trial varying predictor is aligned to an event in a trial: 1) the stereoclick, which defines the start of auditory click trains and the trial itself; 2) the animal's departure from the center port, which ends a trial if it occurs before 1s from the stereoclick; and 3) a neuron's own previous spiking.

On each trial m, the timing of the i-th event is represented by a Delta function, and the predictor at time step t is the linear convolution of the Delta function with a linear filter, or kernel, that is fixed across trials.

$$b(t) = \sum_i k_i * \delta(i, m, t) \tag{42}$$

To reduce model complexity and promote smoothness, for each type of input, the kernel k_i is parametrized as the linear combination of a set of smooth temporal basis functions:

$$k_i = \Phi_i \boldsymbol{w}_i \tag{43}$$

where each Φ_i is a $T \times D$ temporal basis matrix representing D orthogonal temporal basis functions, and $\boldsymbol{w}_i$ is a D-dimensional vector of weights that are learned from the data (see section 4).

bioRxiv preprint doi: https://doi.org/10.1101/2023.10.15.562427; this version posted November 20, 2023. The copyright holder for this preprint (which was not certified by peer review) is the author/funder. All rights reserved. No reuse allowed without permission.

Post-stereoclick kernel The beginning of each trial and the onset of the auditory click trains is indicated by an auditory click played simultaneously by the left and right speaker, i.e., a stereoclick. The kernel k extends from 0-1.0 s after the stereoclick and is parameterized using $D = 5$ basis functions without time warping (see section 4).

Pre-movement kernel This kernel extends from 0.6 s to 0.01 s before the the animal departs from the center port and is parameterized by $D = 2$ temporal basis functions without time warping.

Post-spike kernel This kernel extends from 0.01-0.25 s after each spike emitted by the same neuron (but not by other neurons) and is parametrized by $D = 3$ temporal basis functions with a time warping parameter $\eta_{warp} = 1$.

2.2.3 Decision-independent, across-trial varying predictor

The only decision-independent predictor is that is fixed within each trial is a trial-varying baseline $b^{\text{across}}(m)$, parameterized as the linear combination of eight smooth temporal basis functions evaluated over the start times of each trial m. To reduce the number parameters fit in the MMDDM, the relative weights of up to $D = 8$ smooth temporal basis functions are first learned using a separate linear-gaussian model fit to the firing rates $r(m)$:

$$r(m) \equiv \frac{1}{T_m \Delta t} \sum_{t}^{T_m} y(m,t) \tag{44}$$

where T_m is the number of time steps on the m-th trial, and $\Delta t = 0.01$ s is the duration of each time step in seconds. The linear-gaussian basis function regression model is defined as

$$r \sim \mathcal{N}(\mu, \sigma) \tag{45}$$

$$\mu \sum_{i}^{D} \phi_i(\tau_m) \tag{46}$$

Note that $b^{\text{across}}(m)$ is fixed for all time steps of a trial.

2.3 Behavioral choice

The behavioral choice c is modelled as Bernoulli random variable parametrized by the probability of z at the last time step of each trial. The probability of rightward choice is

$$p(c = 1) = \sum_{z>0} p(z) \tag{47}$$

2.4 Inference

By discretizing the value of z, the MMDDM has the form of an autoregressive, input-output hidden Markov model (HMM) [1]. The "autoregressive" feature refers to the inputs from each neuron's own spike history to capture the long-range correlations between spike train observations of the same neuron, and the "input-output" feature points to the dependence of the spike train observations on multiple baselines that vary on different time scales.

The inference of the most likely parameters of a model of this structure given simultaneously observed spike trains can be efficiently accomplished using the expectation-maximization (EM) algorithm [5]. However, the EM algorithm exhibits slow, first-order convergence when the conditional distributions of the observations, given the latent state, are not well-separated across states [12]. For the MMDDM, a poor separation between the conditional spike train distributions is expected from the approximation of z as many discrete states. Therefore, instead of the EM algorithm, we use the closely related expectation-conjugate-gradient (ECG) algorithm, which shows superior performance for poorly separated conditional distributions [12]. The ECG algorithm computes the exact gradient of the log-likelihood of the observations by solving the expectation step of the standard forward-backward algorithm for HMM's. The gradient can be used by any first-order optimization algorithm to maximize the log-likelihood. The first-order optimization algorithm used here is the limited-memory BFGS [8], which is a quasi-Newton method that efficiently approximates the hessian matrix using the gradients.

bioRxiv preprint doi: https://doi.org/10.1101/2023.10.15.562427; this version posted November 20, 2023. The copyright holder for this preprint (which was not certified by peer review) is the author/funder. All rights reserved. No reuse allowed without permission.

2.4.1 Gradient of the log-likelihood

On each trial, the observations on which the likelihood of the MMDDM parameters are computed consist the behavioral choice c:

$$c = \begin{cases} 0, & \text{left choice} \\ 1, & \text{right choice} \end{cases} \tag{48}$$

and the spike trains N simultaneously recorded neurons:

$$\boldsymbol{Y} = \{y_1, y_2, ...y_N\} \tag{49}$$

$$y = [y_1, y_2, ...y_T]^\top \tag{50}$$

and the spike train of each neuron on each time step $y_{n,t}$ is the spike count of that neuron over $[t, t + \Delta t)$. The gradient of the log-likelihood of the simultaneously recorded spike trains $\boldsymbol{Y}$ and the choice d on each trial is given by

$$\begin{aligned} \nabla \log p(\boldsymbol{Y}, c) &= \frac{\nabla p(\boldsymbol{Y}, c)}{p(\boldsymbol{Y}, c)} \\ &= \frac{\nabla \sum_z p(\boldsymbol{Y}, c, \boldsymbol{z})}{p(\boldsymbol{Y}, c)} \\ &= \frac{\sum_z p(\boldsymbol{Y}, c, \boldsymbol{z}) \nabla \log p(\boldsymbol{Y}, c, \boldsymbol{z})}{p(\boldsymbol{Y}, c)} \\ &= \sum_{\boldsymbol{z}} p(\boldsymbol{z} \mid \boldsymbol{Y}, c) \nabla \log p(\boldsymbol{Y}, c, \boldsymbol{z}) \\ &= \sum_{\boldsymbol{z}} p(\boldsymbol{z} \mid \boldsymbol{Y}, c) \left[\nabla \log p(\boldsymbol{Y}, c \mid \boldsymbol{z}) + \nabla \log p(\boldsymbol{z})\right] \end{aligned} \tag{51}$$

where $\boldsymbol{z}$ is the set of the values of the latent decision variable on each of the T time steps of the trial:

$$\boldsymbol{z} = \{z_1, z_2, ..., z_T\}$$

and conditioning jointly over the latent variable on all time steps. However, because of the first-order Markov dependence, the gradient can be simplified further

$$\begin{aligned} \nabla \log p(\boldsymbol{Y}, c) = &\sum_{z_1} p(z_1 \mid \boldsymbol{Y}, c) \nabla \log p(z_1) + \\ &\sum_{t=2}^{T} \sum_{z_t} p(z_t, z_{t-1} \mid \boldsymbol{Y}, c) \nabla \log p(z_t \mid z_{t-1}) + \\ &\sum_{t=2}^{T} \sum_{z_t} p(z_t \mid \boldsymbol{Y}, c) \sum_{n=1}^{N} \nabla \log p(y_{n,t} \mid z_{t-1}) + \\ &\sum_{z_T} p(z_T \mid \boldsymbol{Y}, c) \nabla \log p(c \mid z_T) \end{aligned} \tag{52}$$

The posterior probabilities $p(z_t \mid \boldsymbol{Y}, c)$ and $p(z_t, z_{t-1} \mid \boldsymbol{Y}, d)$ were computed using the forward-backward algorithm, which can be used even when the spike trains have spike history inputs [5].

2.5 Relationship between MMDDM and rSLDS

The MMDDM can approximately be described in the framework of recurrent switching linear dynamical systems (rSLDS) [6, 15], a model that approximates nonlinear dynamics with a discrete set of linear regimes. The rSLDS framework distinguishes between continuous variables, which we denote here as $\boldsymbol{z}$, and discrete states, which we denote as $\boldsymbol{x}$. The first dimension of the continuous variable $\boldsymbol{z}$ is identical to the one dimensional decision variable in MMDDM. The second dimension of $\boldsymbol{z}$ is close to zero except when the first dimension of $\boldsymbol{z}$ reaches a bound B. The

bioRxiv preprint doi: https://doi.org/10.1101/2023.10.15.562427; this version posted November 20, 2023. The copyright holder for this preprint (which was not certified by peer review) is the author/funder. All rights reserved. No reuse allowed without permission.

two discrete states $\boldsymbol{x} \in \{[1;0],[0;1]\}$ correspond to the dynamical regimes of evidence accumulation ($\boldsymbol{x} = [1;0]$) and decision commitment ($\boldsymbol{x} = [0;1]$):

$$\boldsymbol{x}_t \mid \boldsymbol{x}_{t-1}, \boldsymbol{z}_{t-1} = \begin{cases} [1;0], & \|z_{1,t-1}\| < B \\ [0;1], & \|z_{1,t-1}\| \geq B \end{cases}. \tag{53}$$

Here

$$\boldsymbol{z}_t = \begin{cases} A_1 \boldsymbol{z}_{t-1} + V_1 \boldsymbol{u}_t + \epsilon_{1,t}, & \boldsymbol{x}_t = [1;0] \\ A_2 \boldsymbol{z}_{t-1} + V_2 \boldsymbol{u}_t + \epsilon_{2,t}, & \boldsymbol{x}_t = [0;1] \end{cases}, \tag{54}$$

where $A_1 = [1,0;0;1]$, $V_1 = [1,-1;0,0]$, $\epsilon_{1,t} \sim N(0,[\sigma^2,0;0,10^{-6}])$, $A_2 = [1,0;1,0]$, $V_2 = [0,0;0,0]$, $\epsilon_{2,t} \sim N(0,[10^{-6},0;0,10^{-6}])$. 10^{-6} is some arbitrarily small number.

The initial condition of the $\boldsymbol{z}$ variable is set to be $z_0 = [0,0]$. If there is a bias β in the decision process, then the initial state is $[\beta,0]$. The initial condition of the $\boldsymbol{x}$ variable is $[1;0]$, indicating that the starting regime is always evidence accumulation and not decision commitment.

The mapping from the variable $\boldsymbol{z}$ to the firing rates $\boldsymbol{r}$ of a population of N neurons is given by

$$\boldsymbol{r} = \text{softplus}\,(\boldsymbol{W}\boldsymbol{z} + \boldsymbol{b}) \tag{55}$$

$\boldsymbol{W}$ is a $N \times 2$ matrix in which the first row represents the encoding weights in the evidence accumulation regime (w_{EA}) and the second row the encoding weights in decision commitment minus the encoding weights in the evidence accumulation regime ($w_{DC} - w_{EA}$). The $N \times 1$ vector $\boldsymbol{b}$ represents the decision-irrelevant input, including spike history.

3 Psychophysical kernel model

To test the predictions of MMDDM, we inferred the psychophysical kernel, which quantifies the time-varying weight of the stimulus input on the behavioral choice.

The traditional approach to infer the psychophysical kernel is to use the reverse correlation technique [7], a method highly similar to the spike-triggered average [13]. However, the traditional reverse correlation technique critically depends on the stimulus fluctuations being independent across time. The traditional approach can be biased by inputs that are correlated in time and also biased by stimulus-independent factors that influence the decision but cannot be incorporated in the analysis [10]. Moreover, the traditional technique typically assume a single temporal resolution for the weights of the stimulus fluctuations. When the assumed temporal resolution exceeds what can inferred from the data, the inferred kernel can be highly noisy and has limited interpretability.

We developed a new model, based on logistic regression, to infer the psychophysical kernel that mitigates the bias from sensory inputs with temporally-correlated stimulus fluctuations and the bias from omitted factors that impact the choice. The psychophysical kernel is parametrized using temporal basis functions, and therefore the temporal resolution of the kernel is quantified by the number of basis functions. The optimal number of basis functions for a given dataset can be identified using out-of-sample model comparison.

To mitigate the bias from temporally correlated stimulus fluctuations, we incorporate a method based on the logistic regression model presented in [9] that reparametrizes the inputs to remove the temporal correlations in the stimulus input. To mitigate the potential bias from omitted factors, a behavioral lapse parameter is incorporated. To identify the optimal temporal resolution of the psychophysical kernel that can be inferred using a given data set, the kernel is parametrized as a linear combination of smooth temporal basis functions. Cross-validated model comparison identifies the optimal temporal resolution.

3.1 Model definition

The behavioral choice c is modelled as a Bernoulli random variable. The probability of a right choice is given by

$$p(c = 1) = f(\beta_1)f(\beta_2) + [1 - f(\beta_1)]f(y) \tag{56}$$

where the function f is the logistic function

$$f(x) = \frac{1}{1 + \exp(-x)} \tag{57}$$

bioRxiv preprint doi: https://doi.org/10.1101/2023.10.15.562427; this version posted November 20, 2023. The copyright holder for this preprint (which was not certified by peer review) is the author/funder. All rights reserved. No reuse allowed without permission.

which monotonically maps the input $x \in (-\infty, \infty)$ to the range $(0, 1)$. The value $f(\beta_1)$ quantifies the behavioral lapse rate, or the fraction of trials in which the animal is a behavioral state that ignores the stimulus and depends on only its bias β_2. In the remaining $1 - f(\beta_1)$ of the trials, the choice depends on not only the bias β_2 but also the sensory stimulus. The linear combination of these inputs is given by

$$y = \beta_2 + \beta_3 \lambda T \Delta t + \boldsymbol{e}^\top \Phi \boldsymbol{w} \tag{58}$$

The parameter β_3 is the weight of the expected stimulus input at each time step ($\Delta t = 0.01$), which is represented as $\lambda T \Delta t$. The independent variable λ is the expected stimulus input per second given the random processes used to generate the stimuli on each trial. The hyperparameter T indicates the number of time steps on each trial examined ($T = 40$ when aligned to the time of decision commitment inferred from MMDDM and $T = 75$ when aligned to stimulus onset). When λ does not equal 0, the stimulus fluctuations are temporally correlated across time steps within a trial. Therefore, separate weights are learned for the expected stimulus input and the fluctuations from the expected input.

The expected input rate λ is the difference between the values of right and left input rate expected given the random process used to generate the trial, and the typical expected input rates are $\lambda \in \{-38, -34, -25, -10, 10, 25, 34, 38\}$

Fluctuations from the expected input are quantified as the excess stimulus input $\boldsymbol{e}$. The T dimensional vector $\boldsymbol{e}$ is the difference between the actual and the expected input at each time step τ

$$e(t) = -\lambda \Delta t + \sum_{\tau \in [t - \Delta t, t)} \delta_R(\tau) - \delta_L(\tau) \tag{59}$$

Where $\delta_R(\tau)$ equals 1 when a right click occurred at time τ and is zero otherwise, and $\delta_L(\tau)$ is similarly defined for left clicks.

The weights of the excess stimulus input is given by the vector $\Phi \boldsymbol{w}$. The matrix Φ is $T \times D$. Each row of the matrix Φ corresponds to one of T time step in the trial, and each column consists of the output of one D basis functions (see section 4). The weight vector $\boldsymbol{w}$ has the dimensionality D corresponding to the number of the temporal basis functions, and the values of the vector are learned from the data. When $D = 1$, Φ is constrained to be a vector whose elements are the identical, and the weights $\Phi \boldsymbol{w}$ is constrained to be a flat line.

3.2 Inference

The free parameters of the model are $\{\beta_1, \beta_2, \beta_3, \boldsymbol{w} \in \mathbb{R}^D\}$. The hyperparameter D, which quantifies the number of the temporal basis functions and therefore represents the time resolution of the psychophysical kernel, is optimized by 10-fold cross-validated model comparison.

3.3 Implementation details

3.3.1 Figure 3m

The results shown in Figure 3m are inferred without any basis function. Only trials for which the auditory click trains preceded the moment of out-of-sample MMDDM-inferred decision commitment time by at least 0.2 s and also continued for another 0.2 s were included.

3.3.2 Extended Data Figure 9b-d

The results shown in these panels were from inference using basis functions. Similar to the analysis for Figure 3m, we included only trials for which the auditory click trains both preceded and continued to play after the moment of out-of-sample MMDDM-inferred decision commitment time by at least 0.2 s.

3.3.3 Extended Data Figure 9e-h

To estimate the psychophysical kernel aligned to trial onset (i.e., the start of the auditory click trains), trials with a stimulus duration of at least 0.75s were included from the set of recording sessions used in other analyses.

bioRxiv preprint doi: https://doi.org/10.1101/2023.10.15.562427; this version posted November 20, 2023. The copyright holder for this preprint (which was not certified by peer review) is the author/funder. All rights reserved. No reuse allowed without permission.

4 Basis functions

In either the multi-mode drift-diffusion model (MMDDM) and the psychophysical kernel model, nonlinear basis functions of the independent variables are used to reduce the number of parameters needed to be learned. For a given independent variable whose values vary across T time steps on each trial, we did not learn the weight at each time step. Instead, we learn the weight of each of D basis functions of the independent variable. Because $D << T$, the number of parameters can be greatly reduced.

For a given independent variable, such as the time-varying fluctuations in auditory click input in the psychophysical kernel model, its value on a given trial with T time steps can be expressed as the T-dimensional input vector $\boldsymbol{x}$. The basis function output $\boldsymbol{y}$ of the independent variable is given by

$$\boldsymbol{y} = \Phi^{\top}\boldsymbol{x} \tag{60}$$

The matrix Φ has the dimensions $T \times D$: each column corresponds to an individual basis function, and each row to a time step. The basis function output y is therefore a vector of length D.

The linear combination of $\boldsymbol{y}$ is an input in a pre-nonlinearity stage of either the MMDDM or the PKM. For example, in the MMDDM, the Poisson rate of a neuron $\boldsymbol{\lambda}$ is given by

$$\boldsymbol{\lambda} = h\left(\boldsymbol{w}_1^{\top}\boldsymbol{y}_1 + \boldsymbol{w}_2^{\top}\boldsymbol{y}_2 + ...\right) \tag{61}$$

where h is the softplus function. The linear projection weights $\boldsymbol{w}_i$ are learned for each of the i-th independent variable.

The basis function matrix Φ is pre-specified and fixed for each independent variable and for all trials. Each column of Φ consists of a radial basis function evaluated on the index τ of each time step. The radial basis function we used has the form of a raised cosine [11]. The j-th basis function is given by

$$\phi_j(\tau) = \begin{cases} 1/2 - \cos\left\{\theta_j(\tau)\right\}/2, & \theta \in [0, 2\pi] \\ 0, & \text{otherwise} \end{cases} \tag{62}$$

where the transformation from time step index to radian is given by

$$\theta_j(\tau) = \frac{[f(\tau) - f(1) - (j-3)\Delta]\pi}{2\Delta} \tag{63}$$

The function f is a monotonic time warping function described below. The value Δ is the distance between the peaks of two adjacent basis functions:

$$\Delta = \frac{f(T) - f(1)}{D - 1} \tag{64}$$

After evaluating Φ, it is transformed into a unitary matrix using singular vector decomposition.

4.1 Time warping

To parametrize the post-spike kernel in the MMDDM or the peri-commitment psychophysical kernel, we wish to parametrize the portion of the kernel closer to the event of interest with a higher density of basis functions than the portion of the kernel farther away from the event time. To implement a continuous change in the density of representation, the time step indices are monotonically transformed using the function f

$$f(\tau;\eta) = \sinh^{-1}\{\eta_{warp}(\tau - \tau_0)\} \tag{65}$$

The time index when the event occurred is indicated by τ_0. The parameter η indicates the degree of time warping. The larger is the value of η, the greater the warping: i.e., the portion of the kernel closer to τ_0 is represented by more functions and can have a higher temporal resolution than the portion father away from τ_0. For $1 >> \eta > 0$, the warping is essentially absent, and $f(\tau;\eta_{warp}) \approx \tau$. This can be seen using the first order Taylor approximation of $\text{asinh}^{-1}(\eta_{warp}\tau)$ around zero

$$f(\eta\tau) \approx f(0) + f'(0)\cdot\eta_{warp}\tau = \eta_{warp}\tau$$

bioRxiv preprint doi: https://doi.org/10.1101/2023.10.15.562427; this version posted November 20, 2023. The copyright holder for this preprint (which was not certified by peer review) is the author/funder. All rights reserved. No reuse allowed without permission.

References

[1] C. M. Bishop. *Pattern Recognition and Machine Learning*. Springer Science & Business Media, 2006.

[2] A. D. Brown, G. C. Stecker, and J. T. Daniel. The precedence effect in sound localization. *Journal of the Association for Research in Otolaryngology*, 16, 2015.

[3] B. W. Brunton, M. M. Botvinick, and C. D. Brody. Rats and humans can optimally accumulate evidence for decision-making. *Science*, 340(6128):95–98, 2013.

[4] B. D. DePasquale, J. W. Pillow, and C. D. Brody. Neural population dynamics underlying evidence accumulation in multiple rat brain regions. *bioRxiv*, 2021.

[5] S. Escola, A. Fontanini, D. Katz, and L. Paninski. Hidden markov models for the stimulus-response relationships of multistate neural systems. *Neural Computation*, 23, 2011.

[6] Scott Linderman, Matthew Johnson, Andrew Miller, Ryan Adams, David Blei, and Liam Paninski. Bayesian Learning and Inference in Recurrent Switching Linear Dynamical Systems. In *Proceedings of the 20th International Conference on Artificial Intelligence and Statistics*, volume 54, pages 914–922, 2017.

[7] P. Neri, A. J. Parker, and C. A. Blakemore. Probing the human stereoscopic system with reverse correlation. *Nature*, 1999.

[8] J. Nocedal and S. J. Wright. *Numerical Optimization*. Springer Science & Business Media, 2000.

[9] O. Odoemene, S. Pisupati, H. Nguyen, and A. K. Churchland. Visual evidence accumulation guides decision-making in unrestrained mice. *Journal of Neuroscience*, 2018.

[10] G. Okazawa, L. Sha, B. A. Purcell, and R. Kiani. Psychophysical reverse correlation reflects both sensory and decision-making processes. *Nature Communications*, 2018.

[11] I. M. Park, M. L. Mester, A. C. Huk, and J. W. Pillow. Encoding and decoding in parietal cortex during sensorimotor decision-making. *Nature Neuroscience*, 17, 2014.

[12] R. Salakhutdinov, S. Roweis, and Ghahramani Z. Optimization with em and expectation-conjugate-gradient. *Proceedings of the 20th International Conference on Machine Learning*, 2003.

[13] O. Schwartz, J. W. Pillow, N. C. Rust, and E. P. Simoncelli. Spike-triggered neural characterization. *Journal of Vision*, 2006.

[14] J. D. Yao, P. Bremen, and J. C Middlebrooks. Rat primary auditory cortex is tuned exclusively to the contralateral hemifield. *Journal of Neurophysiolology*, 110, 2013.

[15] David Zoltowski, Jonathan Pillow, and Scott Linderman. A general recurrent state space framework for modeling neural dynamics during decision-making. In *Proceedings of the 37th International Conference on Machine Learning*, volume 119, pages 11680–11691, 2020.